

Master of Science in Geomatics  
Specialisation in Hydrography

## **MASTER THESIS**

# **Development of Digital Bathymetric Models from Hydro acoustic and Photogrammetric Data for Hard to Survey Areas (Shallow and Ultra Shallow Areas)**

by  
**Kwasi Offei-Owusu**

1<sup>st</sup> Examiner: Prof. Dr.-Ing. Harald Sternberg - HafenCity

Universität, Hamburg, Germany

2<sup>nd</sup> Examiner: Markus Kraft - HafenCity

Universität, Hamburg, Germany



### Declaration of Authorship / Affidavit

This declaration has to be submitted together with the thesis

Last name: Offei-Owusu  
First name: Kwasi  
Student number: 6065892  
Degree programme Geodesy and Geoinformatics, Master

Hereby I declare that I have written this thesis with the title

Development of Digital Bathymetric Models from Hydro acoustic and Photogrammetric Data  
for Hard to Survey Areas (Shallow and Ultra Shallow Areas)

without any help from others and without the use of documents and aids other than those stated above. I have mentioned all used sources and cited them correctly according to established academic citation rules.

In the case of group work, the explanation refers to the part of the thesis I worked on.

Hamburg, 17.03.2025

City and Date

Student's signature

A handwritten signature in blue ink, appearing to read "Kwasi Offei-Owusu".

#### TO BE FILLED BY THE EXAMINATION OFFICE

The thesis was submitted on:

Date of Receipt at  
Student Service Center | Examination Office

## Acknowledgement

I express my deepest gratitude to God for granting me the health, wisdom, and strength to complete this course and dissertation successfully.

My heartfelt thanks go to my mother, Ms. Sophia Bonney, for her unwavering support and encouragement throughout this journey.

I am profoundly grateful to Mr. Markus Kraft for his invaluable assistance in securing the necessary permissions from the federal government, which allowed me access to the study site. His guidance and support during the data collection phase were indispensable. I also extend my sincere appreciation to Mr. Lukas Klatt, whose expertise and assistance in acquiring the bathymetric data using his Autonomous Survey Vehicle were crucial to the success of this project.

Finally, I would like to thank everyone who contributed in any way, to my success during this course—whether through direct involvement or moral support. To those whose names I may not have mentioned, please know your contributions are deeply appreciated.

## Abstract

The continuous advancement of technology in the hydrographic industry has significantly enhanced our capability to map shallow and ultra-shallow underwater areas. This study explores the feasibility of using data acquired via drone technology and an Autonomous Survey Vehicle (ASV) to develop a seamless digital bathymetric model for such challenging environments, focusing on the site Boberger See. The Digital Elevation Model (DEM) derived from aerial photogrammetric data of the ultra-shallow portion of the site was integrated with the DEM created from bathymetric data acquired from the shallow portion using the ASV. The integration of these datasets was carried out to generate a seamless and comprehensive bathymetric model. To assess accuracy, the Root Mean Square Error (RMSE) of each dataset was evaluated before integration. This process provided an objective measure of the datasets' precision and their reliability for bathymetric modelling.

**Keywords:** shallow and ultra-shallow waters, bathymetry, photogrammetry, DEM, UAV, ASV

## **Table of Contents**

<b>Acknowledgement.....</b>	<b>II</b>
<b>Abstract.....</b>	<b>III</b>
<b>Table of Contents .....</b>	<b>IV</b>
<b>List of Figures.....</b>	<b>VI</b>
<b>List of Tables .....</b>	<b>VIII</b>
<b>List of Abbreviations .....</b>	<b>IX</b>
<b>1      Introduction .....</b>	<b>1</b>
1.1    Research Objectives .....	2
1.2    Thesis Layout .....	3
<b>2      Background And Literature Review .....</b>	<b>4</b>
2.1    Digital Photogrammetry .....	4
2.1.1 Structure from Motion (SfM) Photogrammetry .....	4
2.1.2 Bathymetric Surveying Using Autonomous Survey Vehicles .....	9
2.2    Instrumentation.....	14
2.2.1 Unmanned Aerial Vehicle (UAV).....	14
2.2.2 Global Navigation Satellite System (GNSS).....	16
2.2.3 Autonomous Hydrographic Survey Vehicle .....	18
<b>3      Methodology.....</b>	<b>21</b>
3.1    Study Area .....	22
3.2    Methodology.....	23
3.2.1 Data Processing .....	27
<b>4      Results And Discussion .....</b>	<b>41</b>

---

4.1	UAV Computation Results.....	41
4.2	Sonobot Data Computation Results.....	59
4.3	Fusion of DEMs .....	63
4.4	Conclusion.....	67
4.5	Recommendation.....	70
<b>5</b>	<b>Summary .....</b>	<b>72</b>
<b>6</b>	<b>Appendix .....</b>	<b>73</b>
	<b>References.....</b>	<b>75</b>

## List of Figures

Figure 1: Structure from Motion Technique (Sweeney, n.d.).....	4
Figure 2:Single Beam Echosounder (Dhabban, 2021) .....	11
Figure 3: DJI Mavic Air 2 (DJI, 2024) .....	15
Figure 4: Trimble R980 (Trimble, 2024).....	17
Figure 5: Autonomous Hydrographic Survey Vehicle (EvoLogics, 2024) .....	19
Figure 6: Methodology flow chart .....	21
Figure 7: Area of Study-Boberger See .....	22
Figure 8: Survey Plan for Boberger See .....	23
Figure 9: Cordoned area of study .....	24
Figure 10: Target on land.....	24
Figure 11: Target on water bed.....	25
Figure 12: Bathymetric data capture using Sonobot 1(ASV) .....	26
Figure 13: Alignment of Aerial Photos.....	27
Figure 14: Import of GCP coordinates .....	28
Figure 15: Computation of Point Cloud .....	30
Figure 16:DEM computation .....	31
Figure 17: Orthomosiac computation .....	31
Figure 18: Bathymetric data captured.....	33
Figure 19: Pattern of altitude of GPS data recorded.....	34
Figure 20: Effect of Depth on GNSS Altitude of ASV .....	37
Figure 21: DEM computation from USV data.....	39
Figure 22: Computation of RMSE.....	40
Figure 23: Point cloud computation output at UAV height 5 m.....	41
Figure 24: DEM before masking (UAV 5 m).....	42
Figure 25: DEM after masking (UAV 5 m).....	42
Figure 26: Camera positions and image overlap (UAV 5 m) .....	43

Figure 27: Camera locations and error estimates (UAV 5 m) .....	44
Figure 28: GCP Locations and error estimates at UAV height 5 m .....	46
Figure 29: Computed Orthomosaic before masking (UAV 5 m) .....	47
Figure 30: Computed Orthomosaic after masking (UAV 5 m) .....	47
Figure 31: Point cloud computation output at UAV height 8 m.....	48
Figure 32: DEM after masking (UAV 8 m).....	49
Figure 33: Camera positions and image overlap (UAV 8 m).....	50
Figure 34: Camera locations and error estimates (UAV 8 m) .....	51
Figure 35: Computed Orthomosaic after masking (UAV 8 m) .....	53
Figure 36: Point cloud computation output at UAV height 10 m.....	54
Figure 37: DEM after masking (UAV 10 m).....	55
Figure 38: Camera positions and image overlap (UAV 10 m) .....	56
Figure 39: Camera locations and error estimates (UAV 10 m) .....	57
Figure 40: Computed Orthomosaic after masking (UAV 10 m) .....	58
Figure 41: DEM computed from ASV data.....	59
Figure 42: Plot of points measured and recorded with their corresponding GNSS mode of measurement .....	60
Figure 43: GNSS assessment during the survey .....	61
Figure 44: ASV DEM after masking .....	63
Figure 45: Final DEM ASV dataset integrated with UAV dataset.....	64
Figure 46: Final DEM ASV dataset integrated with UAV dataset with contours ...	65
Figure 47: 3D Visualized Output of Final DEM ASV dataset integrated with UAV .....	66
Figure 48: DEM before masking (UAV 8 m).....	73
Figure 49: Computed Orthomosaic before masking (UAV 8 m) .....	73
Figure 50: DEM before masking (UAV 10 m).....	74
Figure 51: Computed Orthomosaic before masking (UAV 10 m) .....	74

## **List of Tables**

Table 1: Coordinates Ground Control Points (GCPs) .....	25
Table 2: Control Points RMSE (UAV 5 m).....	44
Table 3: Check Points RMSE (UAV 5 m).....	45
Table 4: Errors Control Points (UAV 5 m).....	45
Table 5: Errors Check Points (UAV 5 m).....	45
Table 6: Control Points RMSE (UAV 8 m).....	51
Table 7: Check Points RMSE (UAV 8 m).....	52
Table 8: Errors Control Points (UAV 8 m).....	52
Table 9: Errors Check Points (UAV 8 m).....	52
Table 10: Control Points RMSE (UAV 10 m).....	55
Table 11: Check Points RMSE (UAV 10 m).....	55
Table 12: Errors Control Points (UAV 10 m).....	57
Table 13: Errors Check Points (UAV 10 m).....	58

## List of Abbreviations

ASV	Autonomous Survey Vehicle
UAV	Unmanned Aerial Vehicle
DEM	Digital Elevation Model
ESRI	Environmental Systems Research Institute
RMSE	Root Mean Square Error
GCPs	Ground Control Points
SBES	Single Beam Echosounder
IDW	Inverse Distance Weighting

## 1 Introduction

Shallow waters are among the most fascinating and heavily utilized areas on Earth. Their accessibility makes them ideal for various purposes, including environmental observation, recreational activities, and tourism. However, they also present significant technological and research challenges. These areas encompass the coastal zones of seas and oceans and inland water bodies like lakes, rivers, and reservoirs. Understanding the shape and structure of the seabed and the surrounding shoreline is crucial for effective coastal zone management and addressing ecological concerns. Over the years, numerous techniques have been developed to map the topography and bathymetry of these regions. Despite this progress, challenges remain, leading to a continuous stream of research and publications proposing innovative solutions (Lubczonk et al., 2021).

Traditionally, data collection in shallow waters relied on manual measurements using a pole. However, as technology advanced, acoustic methods gradually replaced this approach. Initially, single-beam echosounders were introduced, followed by the development of multi-beam echosounders. Today, these hydroacoustic techniques form the foundation of most hydrographic studies, as noted in sources such as (Zwolak et al., 2020) and (Janowski et al., 2021). These techniques tend to deliver the highest level of data accuracy in gathering bathymetric data, such as in (E. Kasvi et al., 2019). They can also be used as the means or standard to which several research works can be referenced in ascertaining the accuracy of the method employed in the research (Yeu et al., 2018) and (Bahaa et al., 2021). Certain research works, such as (Alvarez et al., 2018), have drawn attention to key limitations of these methods, including their time-consuming nature, restricted range in shallow waters, and the intricacy of data processing. This has led to the exploration of alternative bathymetric measurement techniques for coastal zones, such as photogrammetry (primarily using multispectral imaging) and LiDAR technology, which are applied through aerial and satellite systems. The estimation of river depths using remote sensing has historically been based on passive optical imagery (Legleiter et al., 2018).

Numerous studies have demonstrated the effectiveness of passive optical, spectrally-based methods for depth estimation in shallow waters. These techniques are particularly advantageous for mapping large coastal areas where traditional surveys may not be cost-

effective. While they offer reliable results in various scenarios, they also come with certain limitations, primarily due to environmental and technological constraints. Optical methods are susceptible to environmental conditions and are limited to relatively shallow water penetration. Factors such as water turbidity, colour, and atmospheric disturbances can significantly impact the accuracy and feasibility of these measurements (Lubczonk et al., 2021).

Following the previous paragraphs, our capacity to investigate and comprehend underwater topography of shallow and ultra-shallow regions has been dramatically improved by the ongoing progress of technology. This research seeks to explore the creation of a seamless Digital Bathymetric Model (DBM) by the fusion or integration of hydro acoustic and photogrammetric data obtained from these two sensors.

## 1.1 Research Objectives

A thorough comprehension of the topography, including the ocean and the shoreline, is essential for adequately monitoring and utilising coastal zones and resolving ecological challenges. Consequently, several ways have been developed to visually represent the physical attributes and submerged depths in coastal areas and shallow water bodies. Nonetheless, these challenges remain a significant barrier for researchers, leading to the publication of several researches proposing various solutions to mitigate these shortcomings. (Lubczonk, Kazimierski, et al., 2021).

This research seeks the objective of creating a seamless Digital Bathymetric Model (DBM) by fusing data obtained from an Autonomous Survey Vehicle (ASV) fitted with a Single Beam Echosounder and aerial or photogrammetric data obtained using an Unmanned Aerial Vehicle (UAV) equipped with a 48 megapixels camera.

## 1.2 Thesis Layout

The research work is divided into five chapters: Introduction, Background and Literature Review, Materials and Method (Methodology), Results and Discussion and lastly, Conclusion and Recommendations.

Chapter 2 is the Background and Literature Review, which gives an idea of the background of creating Digital Bathymetric Models (DBMs) in relation to the techniques and algorithms used to generate DBMs. Also, a cursory glance at the history of creating DBMs to help appreciate the usefulness of such tasks will be highlighted with a look at case studies where DBMs have been made from multiple sensor systems to help find solutions to shallow and ultra-shallow waters will be catalogued.

Materials and Method (Methodology) constitute the third chapter. This chapter first deals with the instruments and software programs and their accompanying tools and algorithms for data collection and computation of a DBM.

The fourth Chapter, Results and Discussion, contains the results and interpretation of the outcome of the computed DBM. Finally, the last chapter, Conclusion and Recommendations, will provide an outlook on completing the research. At the end of this chapter, the achievement of the research objective is discussed, and recommendations for further work are made.

## 2 Background And Literature Review

### 2.1 Digital Photogrammetry

Digital photogrammetry is a scientific method to extract geometric information about objects from digital images. It is a well-established technique for generating dense 3D point clouds and Digital Elevation Models (DEMs) by analyzing overlapping stereoscopic photos. This approach has been widely applied in various disciplines, including the rapid creation of basin topography maps in hydrological studies. It is commonly utilised in geomorphology to analyse floodplains, identify erosion and deposition patterns, monitor river channel dynamics, measure sediment transport rates, and investigate gravel-bar surfaces and bank erosion. (Alvarez et al., 2018).

#### 2.1.1 Structure from Motion (SfM) Photogrammetry

One of the most prominent photogrammetric techniques is Structure from Motion (SfM), which facilitates the generation of a 3D model by analyzing and processing the camera's motion during image capture (figure 1). Under ideal conditions, where water is transparent and visible in the images, refraction modifications can be implemented to enhance accuracy. (Lubczonk et al., 2021).

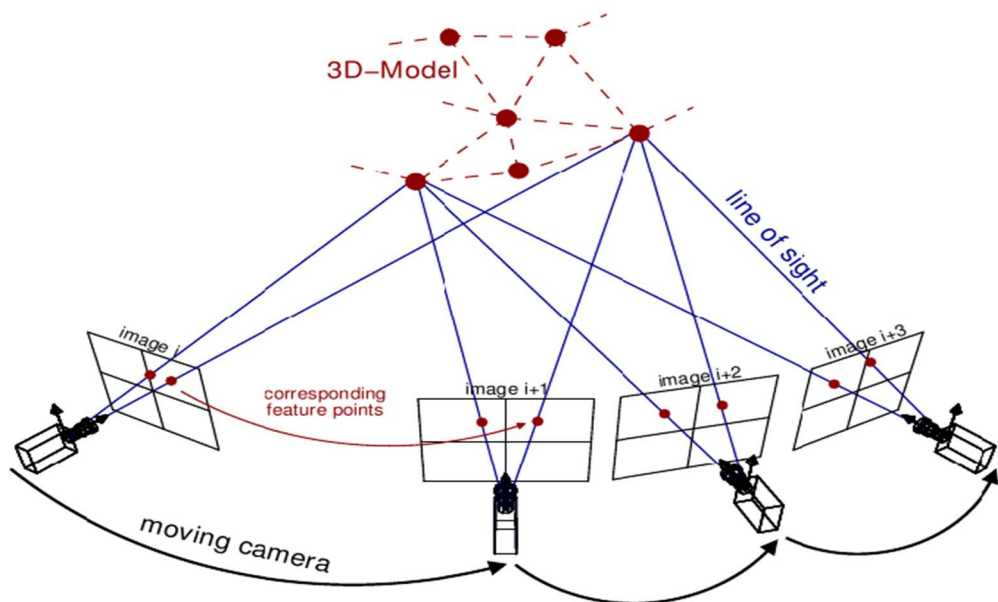


Figure 1: Structure from Motion Technique (Sweeney, n.d.)

This method proves particularly effective for conducting topographic surveys in inaccessible regions. Combining Unmanned Aerial Systems (UAS) with SfM-photogrammetry algorithms provides a cost-effective and efficient solution for generating high-quality Digital Elevation Models (DEMs) in difficult-to-access terrains (Francois Clapuyt et al., 2016).

Although UAS imagery is often geolocated, it lacks accurate scale and orientation. This constraint is typically addressed via georeferencing, which involves aligning the imagery to a defined coordinate system using a number of Ground Control Points (GCPs) with established coordinates. (M.J. Westoby et al., 2012).

After capturing the images, the process of reconstructing a 3D scene and generating a Digital Elevation Model (DEM) commences. To reconstruct a point cloud, it is essential to match key points from three or more overlapping images. Thus, the precision of the 3D point cloud generated using Structure from Motion (SfM) significantly depends on the quality of the aerial photographs collected. This process encompasses tasks such as 3D scene reconstruction and terrain modelling, which require considerable computational resources, similar to the difficulties faced in remote sensing techniques such as LiDAR. Post-Processing Kinematic (PPK) Global Positioning Systems (GPS) are commonly utilized for large-scale surveys to improve the spatial accuracy of photogrammetric models. Software solutions such as Agisoft Metashape, DroneDeploy, and Pix4DMapper Pro employ specialized photogrammetry algorithms that facilitate accurate triangulation and georeferencing, resulting in a precise 3D point cloud. (Alvarez et al., 2018).

Over the past decade, the Structure-from-Motion (SfM) photogrammetry technique has been extensively used in computer vision and visual perception. However, its adoption for mapping landform topography is a more recent development and is still not widely applied to studying underwater terrain (Alvarez et al., 2018).

In their study, (Woodget et al., 2014) evaluated the use of UAS-SfM for generating fluvial topographic models with hyper-spatial resolution (<0.1 m) across two shallow river transects. The rivers had maximum water depths ranging from 0.5 m to 0.7 m. In non-submerged areas, the technique achieved a level of accuracy and resolution comparable to

terrestrial Lidar. For submerged sections, a basic refraction correction was applied, enhancing the accuracy of the DEM. This demonstrated the method's potential for capturing detailed topographic data in shallow, clear-water environments with adequate lighting (Woodget et al., 2014).

(Fonstad et al., 2013) applied the UAS-SfM technique to develop a high-resolution DEM of a bedrock-controlled river system. The image acquisition and processing were carried out using free and open-source software. The study found that the technique achieved accuracy and precision similar to Lidar, with an average deviation of 0.60 m ( $\pm 1.08$  m) while significantly reducing the time and effort required for data collection and processing (Fonstad et al., 2013).

(Bahaa et al., 2021) assessed the accuracy of SRTM15+ V2, a global bathymetric topographic model, using Red Sea floor topography in Egypt. Their study evaluated the vertical accuracy of SRTM15+ V2 constructed from satellite altimetry and shipboard soundings. The model offered a resolution of approximately 500 m x 500 m and was assessed against single-beam echo sounder data across three sites: Abu Zenima, El-Turr and Ain Sokhna. Single-beam echosounder surveys with georeferenced data projected into the same coordinate system as the SRTM model were conducted on these three sites. Root Mean Square Error (RMSE) was the key metric for assessing vertical accuracy. Results from the studies indicated that the site Abu Zenima produced an RMSE value of  $\pm 3.45$  m with a standard deviation of 2.75 m, the site Ain Sokhna produced an RMSE value of  $\pm 2.05$  m with a standard deviation of 2 m and the site El-Turr produced an RMSE value of  $\pm 7.04$  m initially but was reduced to  $\pm 1.10$  m after the correction of a systematic shift in the site data. SRTM15+ V2 demonstrated high vertical accuracy for Abu Zenima and Ain Sokhna, aligning closely with the seafloor topography. After correcting data discrepancies, the site El-Turr also showed improved accuracy. The study concluded that the model suits underwater topography applications within the Red Sea.

In the search for alternatives to traditional empirical and physics-based approaches in the derivation of bathymetric data (Matúš Hodúl et al., 2018) explored the use of Satellite Derived Bathymetry (SDB) using photogrammetry techniques as an approach to obtain bathymetric data. The study was conducted in the Coral Harbour, Nunavut, Canada. Data

was obtained using a photogrammetric method that estimates bathymetry through geometric feature extraction rather than relying on spectral data, making it suitable for areas with heterogeneous seafloors and challenging conditions. The approach involved photogrammetric extraction of stereo WorldView-2 imagery, followed by error removal, refraction correction for underwater depth estimation and tidal reduction to align bathymetric data with local chart datums. The Green band of the imagery, effective for seafloor visibility, was used to derive a 5 m resolution DEM. Corrections addressed the air-water boundary and tidal variations. Validation against Canadian Hydrographic Service survey data showed a mean error of 0.031 m and an RMSE of 1.178 m to depths of approximately 10 m, comparable to SDB methods. The merits of this approach are that, unlike empirical methods, this technique does not require in-situ calibration data. Secondly, the need for radiometric precision, which is required in physics-based methods, is eliminated, making this approach effective in areas with poor atmospheric conditions or limited ground truth data. However, this approach is limited due to the fact that optimal results are obtained when there is the presence of small contrasting benthic features and clear water. Also, this approach struggles with large featureless seafloors and profound depths due to reduced point correlation accuracy. The study concluded that photogrammetric SDB offers comparable accuracy to established methods and is applicable in scenarios where empirical or physics-based approaches are unsuitable. Furthermore, this method holds promise for cost-effective and spatially extensive bathymetric mapping, particularly in challenging environments.

Similar to the work by (Matúš Hodúl et al., 2018), (Arun et al., 2021) used Sentinel-2 Satellite imagery to estimate nearshore bathymetry. They compared traditional empirical models (Log-Ratio Model, LRM; Log-Linear Model, LLM), ensemble techniques and machine learning (Support Vector Regression, SVR) to improve bathymetric accuracy for coastal applications. Rushikonda Bay in India was the study area. In-situ depth data was collected using a Jet Ski-based echosounder. Results obtained indicated that the LLM provided better accuracy and smoother results than the LRM, especially in shallow waters (0-12 m) of depth.

Additionally, the LLM achieved lower RMSE compared to the LRM. The ensemble method reduced noise by combining multiple images, resulting in improved depth estimates compared to single-scene imagery. Also, the LLM ensemble outperformed the LRM ensemble, demonstrating smoother and more accurate depth retrievals. The Support Vector Regression (SVR) applied to both LRM and LLM significantly enhanced accuracy with RMSE values of 0.57 m (LRM-SVR) and 0.39 m (LLM-SVR). SVR effectively handled nonlinear relationships and variable environmental conditions, making it the study's most reliable method for bathymetry estimation. The study demonstrated the potential of SVR-based satellite-derived bathymetry (SDB) for creating high-resolution bathymetric maps to support coastal research, navigation, and environmental management. The study concluded that the SVR approach, particularly with the LLM, outperformed traditional empirical and ensemble methods, offering a robust tool for nearshore bathymetric mapping in shallow coastal waters. The findings underscore the importance of machine learning in improving the accuracy and reliability of satellite-derived bathymetry.

(Alvarez et al., 2018) present an innovative methodology that combines Unmanned Aerial Systems (UAS)-based imagery, echo sounding, and adaptive sampling to address challenges in bathymetric surveys. Their approach merges two techniques: (1) single-beam echosounder measurements collected via a miniaturized, UAS-towed boat for deeper areas, and (2) Structure from Motion (SfM) photogrammetry to extract data from shallower, visible zones. The integration is facilitated by a zonal adaptive sampling algorithm, which improves data density in regions with high spatial variability, enhancing the overall accuracy of the bathymetric dataset.

The technique was validated in a small reservoir in Oklahoma, achieving strong correlations between field measurements and the hybrid bathymetric survey. Results indicated centimetre-level accuracy, with the adaptive sampling algorithm reducing errors and improving efficiency. The study emphasized the cost-effectiveness and flexibility of this method compared to traditional techniques, which are resource-intensive and limited in scope.

(Savio et al., 2023) researched the approach of conducting bathymetric surveys in shallow water environments using Unmanned Aerial Vehicles (UAVs) equipped with photogrammetry. The study, performed in a controlled setting, explored the impact of environmental variables such as turbidity and luminosity on survey accuracy. The authors evaluated the method by conducting 26 UAV flights over a  $67.5 \text{ m}^2$  swimming pool under various controlled conditions, including clear and turbid water, and compared the results against conventional topographic surveys.

The study identified that environmental factors significantly influence errors in in-depth measurements:

- a. At depths up to 0.97 m, higher luminosity minimized errors.
- b. Increased turbidity enhanced accuracy in depths  $\leq 0.49 \text{ m}$  but caused errors to rise beyond this threshold, aligning with optical distortion caused by suspended particles.

UAV-based photogrammetry produced accurate point clouds and Digital Elevation Models (DEMs) comparable to traditional methods while offering advantages in terms of cost, accessibility, and operational ease. Flights at 30 m altitude yielded better resolution than those at 50 m, demonstrating the importance of flight parameters in survey precision.

The research underscored the adaptability of UAV technology in bathymetric studies, particularly in environments where traditional methods are cost-prohibitive or logistically challenging. However, it also highlighted limitations under extreme turbidity, suggesting the need for further refinement in processing algorithms for such conditions.

### **2.1.2 Bathymetric Surveying Using Autonomous Survey Vehicles**

An Autonomous Surface Vehicle (ASV) equipped with a single beam echo sounder (SBES) combines the autonomous navigation capabilities of the ASV with the acoustic depth-measuring capabilities of the SBES. The SBES mounted on the ASV emits a short acoustic pulse (sound wave) downward through the water column. The sound wave travels through the water until it encounters the seafloor or another reflecting surface, where it is reflected back to the transducer as an echo (figure 2). The SBES records the time interval ( $t$ ) between the emission and reception of the sound wave.

$$d = \frac{v \cdot t}{2}$$

equation 1

Where:

v: speed of sound in water

t: round trip travel time

the depth (d) of the water column beneath the ASV is calculated using the formula in equation 1.

The speed of sound is influenced by environmental factors such as water temperature, salinity, and pressure, which are accounted for using sound velocity profiles or onboard sensors.

The ASV's GNSS system provides georeferenced positional data, ensuring that the depth measurements from the SBES are associated with precise geographic coordinates. As the ASV moves along its pre-programmed or autonomously navigated survey path, the SBES emits a narrow conical beam, recording depth data at single points beneath the ASV. These individual measurements are aggregated to produce a continuous depth profile of the survey area. The ASV's autonomous capabilities allow it to operate in shallow or hard-to-reach areas, where traditional survey vessels might face challenges. Integrating an SBES on an ASV provides a cost-effective and efficient solution for hydrographic surveys, ensuring high-precision, in-depth measurements and georeferenced data acquisition. However, the accuracy of the measurements depends on the proper calibration of the SBES, the correction of environmental variables, and the compensation for ASV motion, such as pitch, roll, and heave (EvoLogics, 2024).

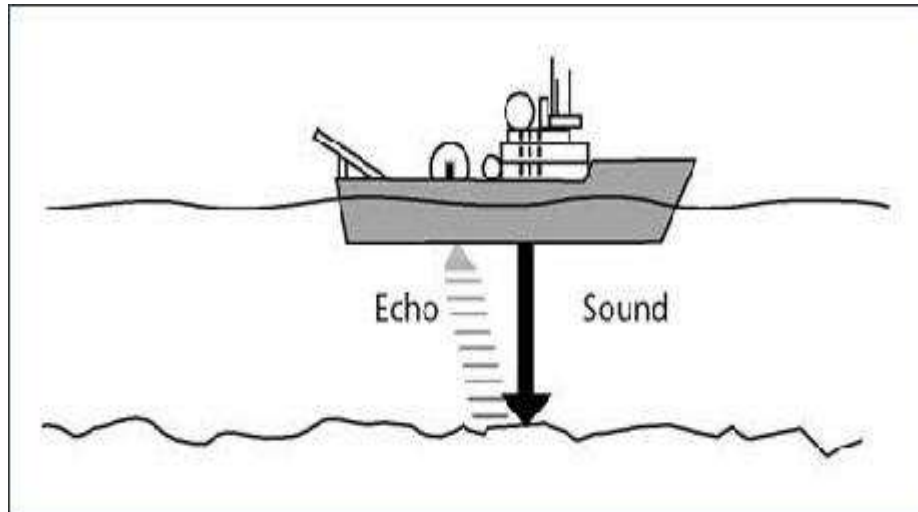


Figure 2:Single Beam Echosounder (Dhabban, 2021)

ASVs are increasingly used in hydrographic surveys to overcome the challenges of shallow and hard-to-reach water bodies. The catamaran-based ASV discussed in this study was designed for stability and operational efficiency in shallow environments. Combining autonomous operation with advanced sonar and navigation systems, ASVs provide detailed bathymetric data at a fraction of the cost of traditional hydrographic vessels. Their ability to operate autonomously minimizes human intervention, enhancing efficiency and adaptability for various survey conditions.

The ASV in this study incorporated several innovative design elements. A catamaran hull was selected for its stability, reduced hydrodynamic drag, and shallow draft, making it ideal for surveys in areas with minimal depth. The ASV was equipped with a Humminbird Helix 5 CHIRP Side Imaging (SI) Sonar, capable of dual-beam and side-scan functionality, ensuring precise and detailed data collection in shallow waters. For navigation and control, a PixHawk controller and a Ublox Neo-M8N GNSS module provided accurate geolocation and autonomous navigation capabilities. Pre-survey calibration was conducted in a controlled swimming pool environment to fine-tune the sonar and navigation systems, correcting depth offsets using known reference points.

The case study involved the bathymetric survey of Powai Lake, an artificial freshwater lake in Mumbai, India. The ASV successfully mapped large portions of the lake despite

challenges such as aquatic vegetation. The collected data were processed using specialized software (ReefMaster) to generate bathymetric maps, visualize depth variations, and calculate water volume and surface area. The survey results were comprehensive: the ASV mapped an area of 1,765,845 square meters, determined a total water volume of 3,782,966 cubic meters, and identified an average depth of 2.1 meters and a maximum depth of 5.83 meters. A depth-volume analysis provided further insights, showing the lake's water volume at 1-meter depth intervals, critical for hydrological and environmental assessments.

The study demonstrated several advantages of ASVs over traditional survey methods. The ASV's cost-effectiveness was evident in its compact design and affordable components, significantly reducing operational expenses. Its autonomous operation enabled surveys in inaccessible or dangerous areas with minimal human intervention. The sonar and GNSS systems ensured high accuracy, while the modular design allowed for adaptability to various survey conditions. These features make ASVs particularly suitable for dynamic shallow water environments where traditional methods may struggle.

Despite its success, the study identified certain limitations. Aquatic vegetation in parts of Powai Lake hindered data collection in some areas. Additionally, while the ASV was autonomous in navigation, it relied on manual intervention for mission planning and sensor calibration. Future improvements, such as advanced mission planning algorithms and enhanced sensor independence, could further optimize the ASV's performance and reduce human involvement.

In conclusion, the study highlighted the potential of Autonomous Surface Vehicles as a practical and cost-effective solution for shallow water bathymetric surveys. The ASV demonstrated its ability to generate accurate bathymetric maps and perform hydrological analyses, making it a valuable tool for environmental monitoring, resource management, and research. By addressing the identified limitations and incorporating advanced technologies, ASV-based bathymetry can be vital in enhancing hydrographic survey practices globally (Wilson et al., 2022).

In the research carried out by (Manda et al., 2015), they used a low-cost and flexible system for autonomous surface vehicle (ASV)-based hydrographic surveys designed to

minimize expenses while maximizing functionality. It leverages mass-produced hardware and open-source software to provide an affordable and efficient solution for hydrographic operations. The system was specifically designed for integration into small ASVs, making it suitable for low-budget applications in shallow water environments.

The system combines commercially available hardware, such as the BeagleBone Black embedded Linux computer and Arduino Mega microcontroller, to perform autonomous navigation and data acquisition tasks. It includes long-range Wi-Fi for communication, GPS/INS modules for precise positioning, and optional integration of sonar systems. The platform also employed open-source software, specifically the MOOS-IvP autonomy framework, which supports mission-oriented behaviours like waypoint navigation, collision avoidance, and hydrographic survey operations.

The total system cost was under \$1,000, significantly lower than traditional ASV solutions, often exceeding \$50,000. The modular design allowed the system to be adapted to various ASV platforms and operational requirements. Open-source software and widely available hardware components ensured ease of development and customization. Integration of efficient power systems supported long-duration missions, with the option to add more power sources for extended surveys.

The system was initially tested on NOAA's EMILY ASV, a 1.7-meter gas-powered vehicle. The platform included pre-programmed behaviours for hydrographic surveys, such as "lawnmower" pattern navigation and depth-adaptive path planning. It was validated in simulations and bench tests, demonstrating the feasibility of conducting hydrographic surveys in low-traffic, nearshore environments.

The system's functionality was limited to single-beam sonar, requiring further testing in real-world conditions. Future improvements aim to integrate multibeam sonar systems, enhance path-planning algorithms, and deploy the ASV in more dynamic environments, such as high-current nearshore or open ocean regions.

The Pladypos Autonomous Surface Vehicle (ASV) was developed as a cost-effective and efficient platform for underwater archaeological surveys, focusing on documenting submerged structures at Caesarea Maritima, Israel. Designed for shallow-water applications,

the Pladypos features an overactuated hull with four thrusters for precise manoeuvrability, enabling it to perform pre-programmed survey missions such as lawnmower patterns. Equipped with high-precision GPS, a 9-axis INS, a Doppler Velocity Logger (DVL), and imaging tools like low-light mono cameras, the ASV collects georeferenced bathymetric and optical data for producing detailed 2.5D models and photomosaics. In field experiments, the Pladypos successfully surveyed Caesarea's inner and outer harbours, generating high-resolution maps of Roman and Crusader ruins and submerged breakwaters at depths ranging from 1 to 8 meters. The ASV demonstrated significant advantages, including reduced survey time, high-quality data suitable for GIS integration, and operational flexibility in challenging environmental conditions, all while minimizing costs by eliminating the need for expensive support vessels. Challenges such as limited DVL point cloud resolution and the labour-intensive alignment of optical and telemetry data were identified, with future improvements planned to incorporate high-resolution multibeam sonar and extend operational capabilities to deeper waters. The Pladypos ASV represents a transformative advancement in underwater archaeological methodology, providing an affordable and efficient solution for documenting submerged cultural heritage sites (Vasiljevic et al., 2015).

## 2.2 Instrumentation

Three instruments were deployed for data capture during this study. An Unmanned Aerial Vehicle (UAV) DJI Mavic Air 2 to capture aerial images for digital photogrammetry, a Trimble R980 GNSS receiver for target(s) or Ground Control Points position capture and an Autonomous Survey Vehicle (Sonobot 1) manufactured by Evo Logics for the capture of sounding data.

### 2.2.1 Unmanned Aerial Vehicle (UAV)

The DJI Mavic Air 2 UAV -figure 3 - was announced on April 27<sup>th</sup> 2020. This new UAV represented a significant advancement in DJI's line-up of consumer drones. Building upon the foundation laid by the original Mavic Air, the Mavic Air 2 offered enhanced features tailored for both enthusiasts and professionals (DJI, 2020).



Figure 3: DJI Mavic Air 2 (DJI, 2024)

The Mavic Air 2 showcases a design evolution, aligning more closely with the Mavic 2 series. It features foldable arms for increased portability and a weight of approximately 570 grams, balancing portability with advanced functionality (Murphy, 2020).

Equipped with a 1/2-inch CMOS sensor, the Mavic Air 2 captures 12-megapixel images and introduces a 48-megapixel mode for higher-resolution shots. It is DJI's first drone to offer 4K video recording at 60 frames per second with a 120 Mbps bitrate, enabling smooth and detailed footage. Additionally, the drone supports 1080p slow-motion video at 120 and 240 fps, catering to creative videography needs (Gilbertson, 2020).

The drone boasts a maximum flight time of up to 34 minutes, providing extended aerial sessions for capturing content. Its top speed reaches approximately 68.4 kilometres per hour (42.5 miles per hour), matching its predecessor while maintaining stability and control (DroneDJ, 2020).

The DJI Mavic Air 2 incorporates innovative safety features aimed at ensuring a secure and reliable flying experience. It is equipped with obstacle sensors positioned at the front and rear, alerting pilots when the drone approaches an object. These sensors can also be configured to stop the drone to prevent collisions automatically. Additionally, the drone features auxiliary lights and sensors on its underside, which facilitate smooth and precise landings, even in challenging lighting conditions. The Mavic Air 2 also integrates GEO geofencing technology to restrict flight near high-risk areas, such as airports, enhancing operational safety.

The Advanced Pilot Assistance System (APAS) 3.0 enhances the drone's autonomous flight capabilities. Upon activation, APAS 3.0 enables the Mavic Air 2 to manoeuvre around, above, or beneath impediments in its trajectory, allowing pilots to concentrate on image capture in intricate settings. This enhanced system utilises 3D mapping technology to guarantee seamless transitions and fluid motions, especially in complex environments with multiple barriers.

Aligned with DJI's 10-point Elevating Safety vision, the Mavic Air 2 is the first consumer drone from DJI to feature AirSense technology. This system enhances situational awareness by using aviation technology, ADS-B, to detect nearby aircraft such as aeroplanes and helicopters. It provides real-time alerts to the drone pilot through visual notifications, sounds, and vibrations, promoting safer navigation by enabling timely evasive actions (DJI, 2020).

### **2.2.2 Global Navigation Satellite System (GNSS)**

The Trimble R980 – figure 4 - is a premium Global Navigation Satellite System (GNSS) receiver engineered to deliver exceptional accuracy and productivity for surveying professionals, particularly in challenging environments.



Figure 4: Trimble R980 (Trimble, 2024)

The Trimble ProPoint GNSS technology is at the core of the R980, enabling exceptional satellite tracking in areas with signal obstructions, such as dense foliage, urban environments, or near structures. It ensures robust performance where traditional GNSS systems may struggle.

The Trimble Inertial Platform (TIP) integrates an inertial measurement unit (IMU) to allow tilt compensation. Surveyors can collect accurate measurements without the need to hold the survey pole perfectly vertically, improving productivity in tight or uneven spaces.

The R980 offers multiple connectivity options, including a dual-band 450/900 MHz UHF radio and a global 4G LTE modem. These features support seamless communication for real-time data transfer and access to correction services over extended ranges.

The system onboard the Trimble R980 supports Real-Time Kinematic (RTK) positioning, achieving centimetre-level accuracy. Additionally, it is compatible with Trimble Center-Point RTX correction services, which provide precise corrections globally without requiring a base station.

All major constellations, including GPS, GLONASS, Galileo, BeiDou, QZSS, and NavIC, with 672-channel tracking capability for comprehensive coverage, are supported by the R980.

Horizontal accuracy of  $8 \text{ mm} + 1 \text{ ppm}$  and vertical accuracy of  $15 \text{ mm} + 1 \text{ ppm}$  is achievable.

Tilt compensation is achieved by adding a 5 mm horizontal error plus 0.4 mm per degree of tilt (up to  $30^\circ$ ).

The R980 is built for rugged environments. The receiver meets IP67 water and dust resistance standards and is lightweight at approximately 1.13 kg.

For safety and reliability, the Trimble R980 incorporates a spectrum analyzer to detect and mitigate interference such as GNSS jamming or spoofing. This ensures the integrity of positioning data in sensitive or contested environments (Trimble, 2024).

### 2.2.3 Autonomous Hydrographic Survey Vehicle

The Sonobot 1- figure 5 - developed by EvoLogics, is an autonomous hydrographic survey vehicle designed for efficient data collection in harbours and inland waters.



Figure 5: Autonomous Hydrographic Survey Vehicle (EvoLogics, 2024)

The Sonobot 1 features a catamaran design with carbon fibre floaters and integrated hydro-jet thrusters, ensuring stability and manoeuvrability. Its lightweight construction allows for single-person handling and transport, fitting conveniently into a car trunk.

Equipped with an autopilot system, the vehicle can execute pre-programmed survey missions autonomously. It also offers remote control capabilities via Wi-Fi, providing flexibility in various operational scenarios.

The Sonobot 1 comes with a single-beam echo sounder utilizing EvoLogics' patented S2C broadband communication technology for precise depth measurements, even in shallow waters. It operates within a frequency range of 80 kHz to 120 kHz, capable of measuring depths from a minimum of 0.5 meters to a maximum of 60 meters. The achievable accuracy of this system is approximately 6 millimetres, ensuring precise bathymetric data collection. Optional sensors include side-scan sonar for detailed imaging and a high-precision differential GPS (supporting GPS, GLONASS, and Galileo) for accurate positioning. The positioning system provides horizontal accuracy within  $\pm 4$  centimetres and vertical accuracy within  $\pm 2$  centimetres when utilizing Real-Time Kinematic (RTK) corrections. Powered by batteries that support over 10 hours of operation at optimal speed, the Sonobot 1 is well-suited for extensive survey missions without frequent recharging.

The vehicle features onboard data logging with wireless transmission capabilities, allowing real-time data access and processing. The accompanying software (Neptus) provides visual georeferenced representations, facilitating efficient field operations and data analysis (EvoLogics, 2024).

### 3 Methodology

Figure 6 is a flow chart showing the methodology used. It consists of four general steps: selection of the study area, data collection, data processing and analysis.

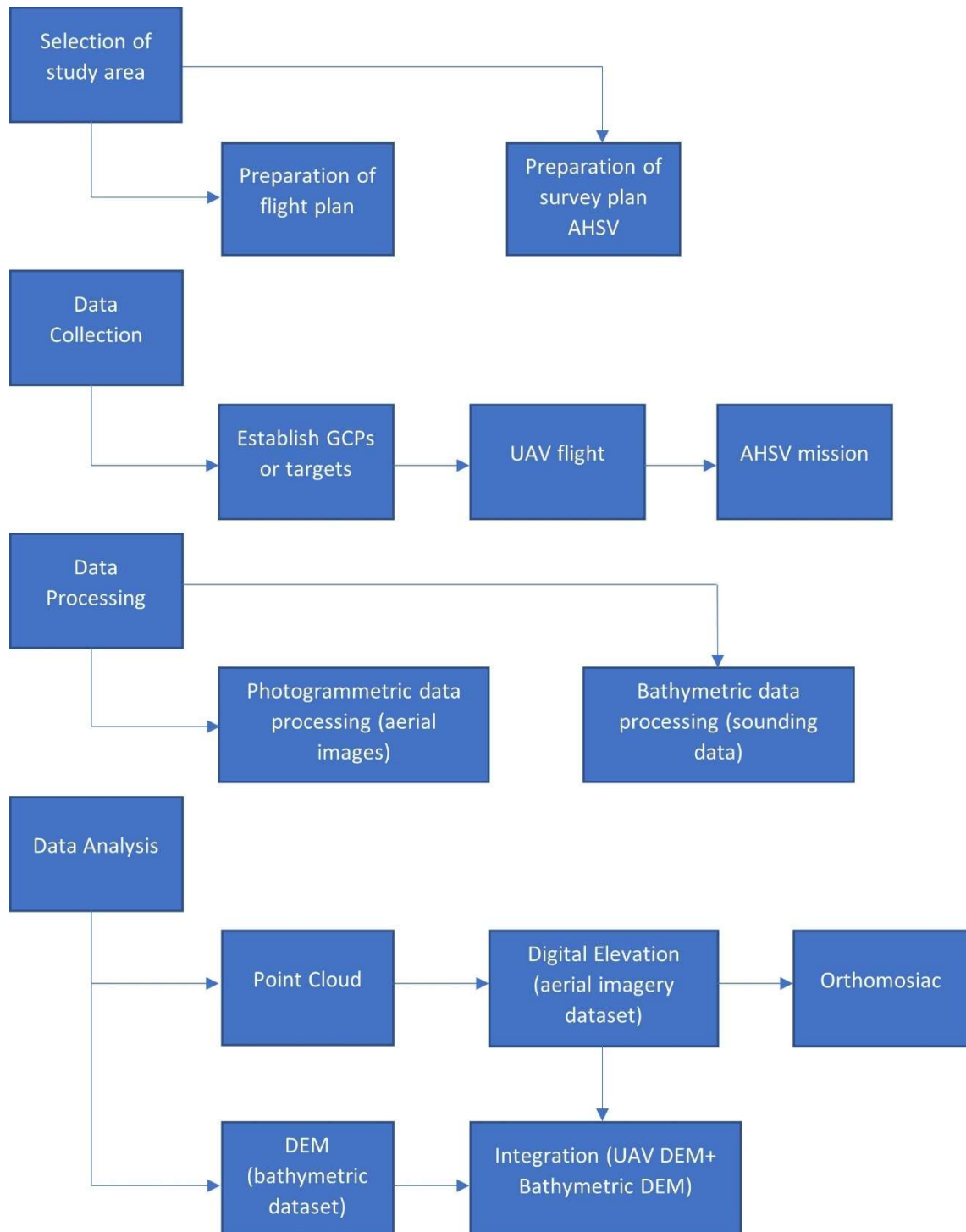


Figure 6: Methodology flow chart

### 3.1 Study Area

The study area chosen for this project is the Boberger See (figure 7). Boberger See is an artificial lake situated within the Boberger Niederung nature reserve in Hamburg. The lake was formed around 1937 through sand excavation to construct the nearby Hamburg-Lübeck section of the former Reichsautobahn. It covers an area of approximately 7.86 hectares, with a maximum depth of about 11 meters. The lake is, on average, about 330 meters long and 170 meters wide, including individual bays and a long, narrow tip, with maximum dimensions of 486 meters in a north-westerly and 392 meters in a south-west-westerly direction (Hamburg Tourismus, 2024).

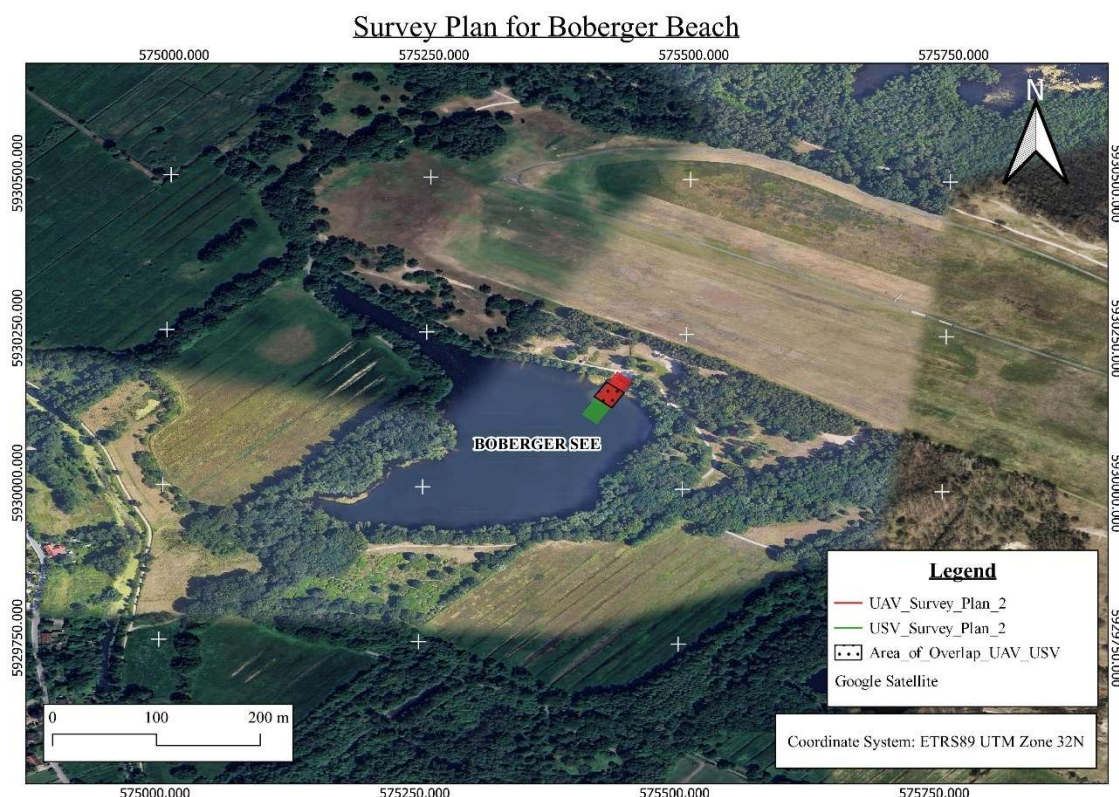


Figure 7: Area of Study-Boberger See

This area was chosen for study because the clarity of water was appropriate for the study. Additionally, the shallow and ultra-shallow portion of the lake was most suitable for the study.

### 3.2 Methodology

Upon identifying an ideal area of study, a survey plan (figure 8) was then drawn up. This involved flying and capturing aerial images along 8 flight lines. The interval between these lines was planned to be 2.5 m, ensuring a 100% overlap of the images captured. Ground control points (GCPs) were intended to be established 10 m along and 10 m across these flight lines. Establishing the position of these GCPs- Eastern (s) and Northern(s)- will be done using the Trimble GNSS survey instrument. Bathymetric data will be captured using the Sonobot 1 by Evo Logics. This data will be captured along 8 track lines running in line with the 8 flight lines. However, these track lines will proceed further into the water body, as shown in figure 8. The UAV flight plan was drawn up so that it would capture data at the ultra-shallow portion of the lake, whilst ASV would capture data at the shallow portion.

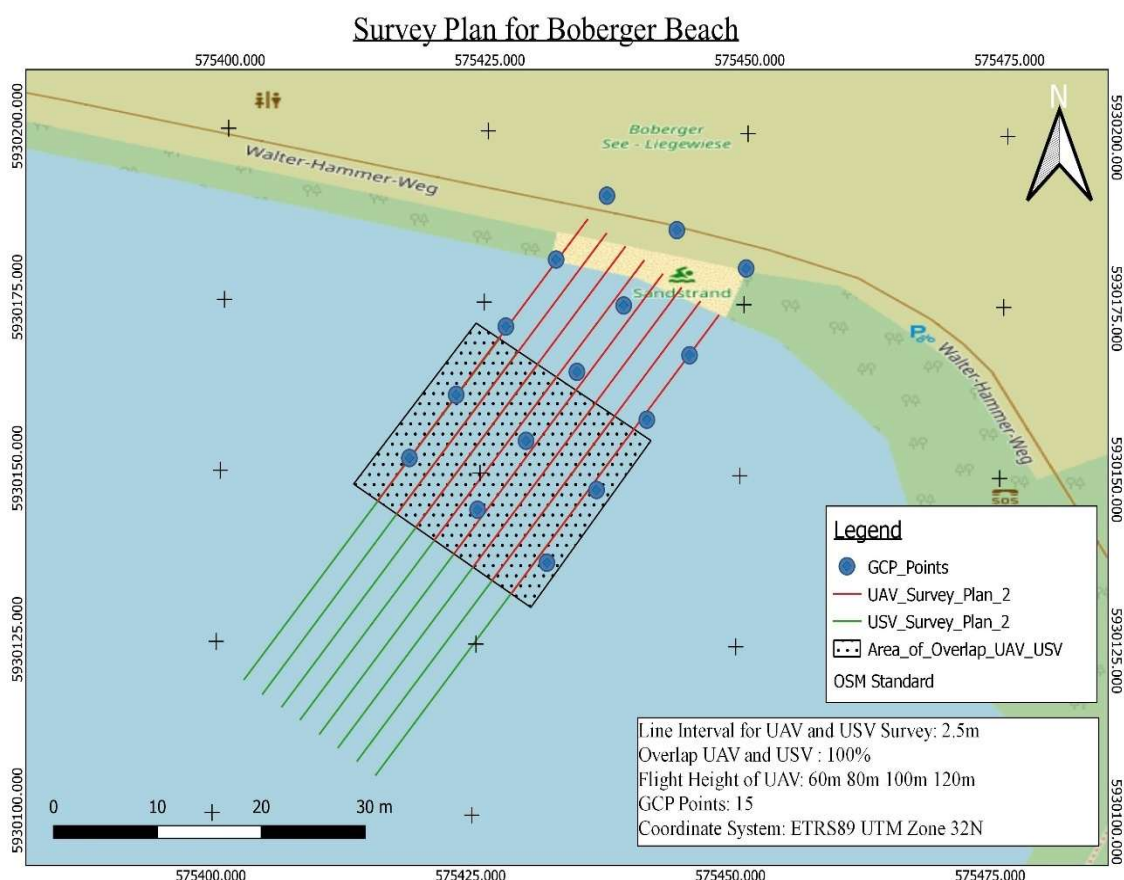


Figure 8: Survey Plan for Boberger See

Capturing aerial data accurately required cordoning off the area of the study, which was done, as can be seen in figure 9. Data was captured mid-morning to ensure calm waters and the non-presence of visitors at the lake



Figure 9: Cordoned area of study

Prior to the capture of aerial data GCP's targets as shown in figures 10 and 11 were placed at positions 10 m along and 10 m across the planned flight lines.

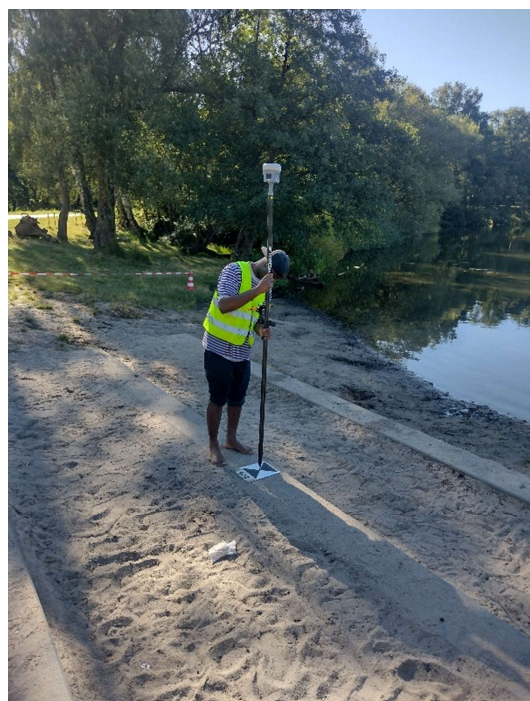


Figure 10: Target on land

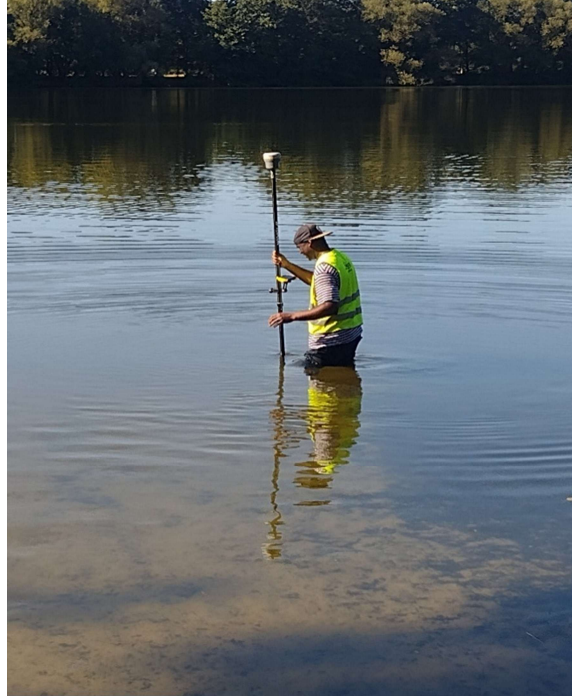


Figure 11: Target on water bed

Three of these metal targets (GCPs) were placed on dry, and the remaining four were placed on the water bed. The positions – Eastern(s) and Northern(s)- were measured using Trimble GNSS R980, as observed in table 1 below. Coordinates were measured in the ETRS89 UTM Zone 32N coordinate system with vertical height reference based on Deutsches Haupthöhennetz 2016 (DHHN2016) or GCG2016, whilst aerial data was captured in the WGS84 EPSG 4326 coordinate system.

No.	Longitude	Latitude	Altitude
908	10.137714	53.515191	1.36
902	10.137728	53.515146	0.638
907	10.137668	53.515164	0.65
906	10.137529	53.515049	-0.885
904	10.137543	53.515013	-1.046
909	10.137633	53.514985	-1.046
806	10.137678	53.514985	-0.933

Table 1: Coordinates Ground Control Points (GCPs)

Aerial images were then captured at flight heights of 10 m, 8 m, 5 m along 8 flight lines with an interval of 2.5 m, enabling 100% overlap to be attained.

Bathymetric data was obtained using the Sonobot 1 Autonomous Hydrographic Survey Vehicle manufactured by Evo Logics (figure 12). The accompanying software (Neptus) enabled real-time visualization of captured data, as shown in figure 12 below.

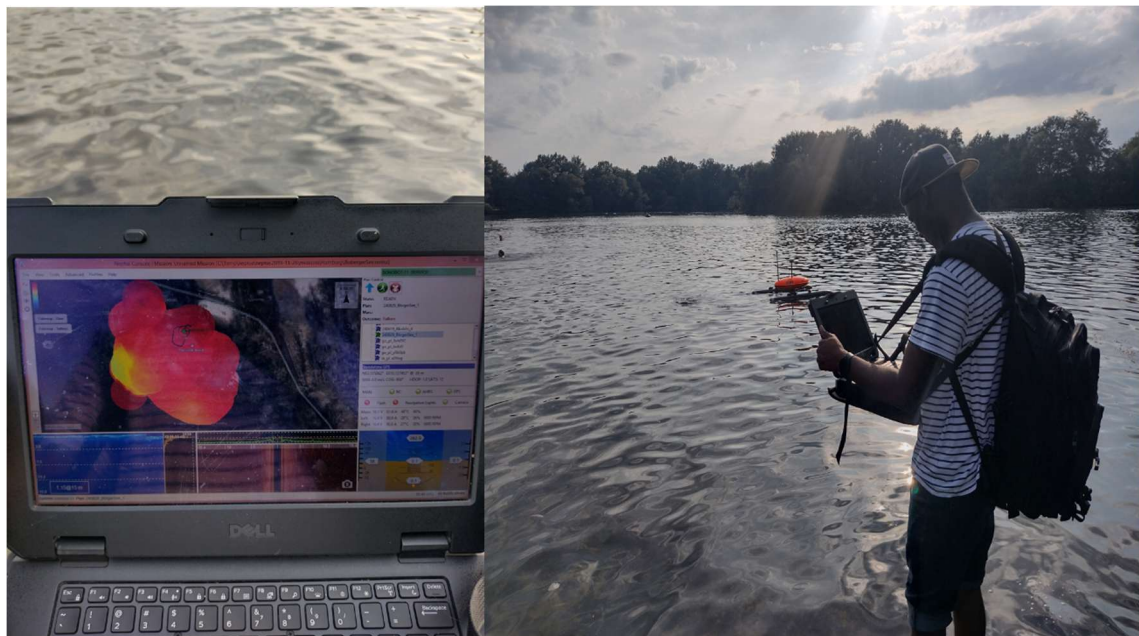


Figure 12: Bathymetric data capture using Sonobot 1(ASV)

Navigation during data capture was facilitated by a Javad-GNSS receiver installed on the Sonobot 1. The fix type ranged from Autonomous Accuracy (AA), Real-Time Kinematic Float Solution (FF) to Full Fix or RTK Fixed Solution (RR). AA indicates a GPS fix obtained autonomously without correction data. This mode relies solely on satellite signals without additional support like Differential GPS (DGPS) or Real-Time Kinematic (RTK) corrections. Accuracy is generally lower compared to corrected positioning modes but sufficient for basic navigation in open areas. Horizontal accuracy of approximately 1 m can be achieved with this mode. FF indicates a GNSS fix using partial or incomplete RTK corrections. In this mode, the receiver is receiving some RTK correction data, but the solution is not yet fully resolved (i.e., the ambiguities in the satellite signals are not completely fixed). Accuracy is better than autonomous mode but not as precise as a Full RTK fixed solution. The possible achievable horizontal accuracy is approximately 2 cm.

RR indicates the highest level of positioning accuracy, achieved when the GPS receiver resolves all ambiguities in the satellite signals using RTK corrections.

In this mode, base station or network corrections are applied to refine the position, offering centimetre-level precision. This mode is ideal for applications requiring very high accuracy, such as bathymetric surveys. Horizontal accuracy of approximately 2 cm is achievable. Onboard Sonobot 1 was a Javad GNSS receiver. Data was captured using the mode RR. The Vertical Root Mean Squared Error (RMSE) of data captured by the GNSS system onboard Sonobot 1 ranged from 0.74 m – 1.05 m. Data captured using the Sonobot 1 was done in the WGS84 EPSG:4326 coordinate system. Height readings were based on the WGS84 ellipsoid at the fixed water level of 39.86 m NHN (Normalhöhennull).

### 3.2.1 Data Processing

Aerial photos captured with the UAV were processed with the Agisoft Metashape Software version 2.1.4. The alignment of data captured was processed utilizing the parameters observed in figure 13 below.

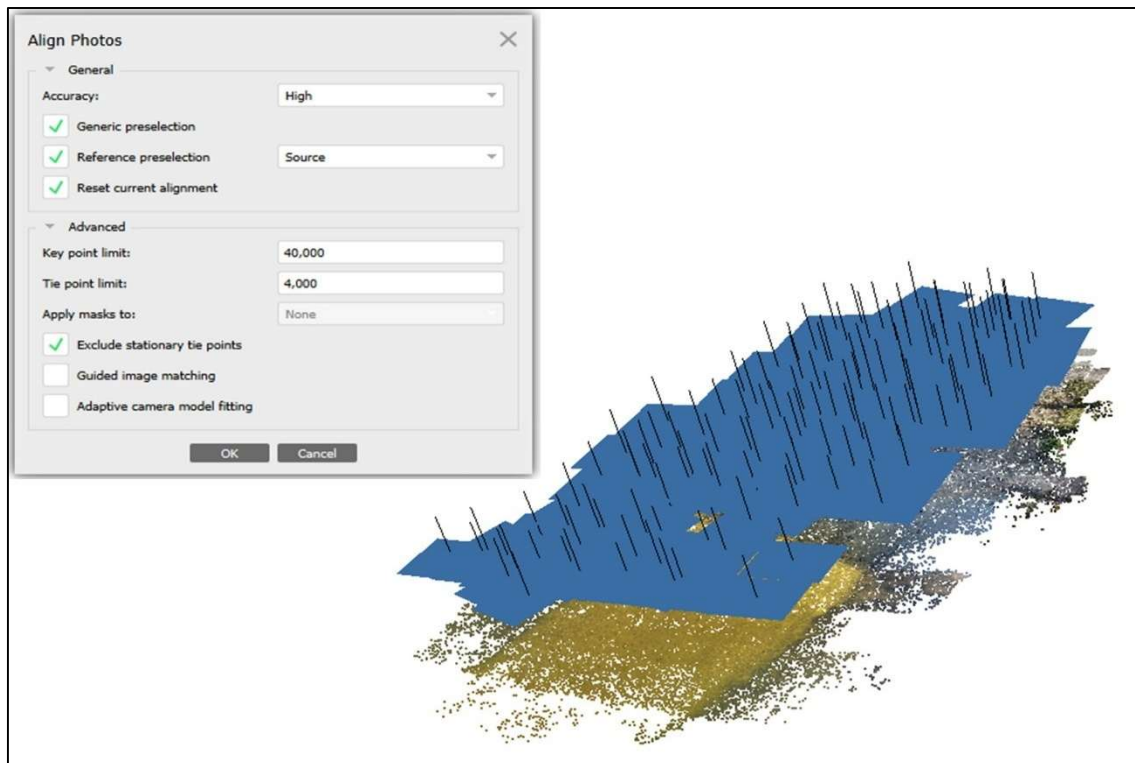


Figure 13: Alignment of Aerial Photos

High accuracy was chosen to ensure high quality feature detection leading to optimal alignment of photos. Generic and reference preselection were utilized to narrow down the photo pairs that are compared thereby improving efficiency. Choosing source ensured that the alignment aligned with the real-world georeferenced data. The limit for key point limit and tie point limit were set to 40,000 and 4,000, respectively, to ensure that an adequate number of features per points are detected per image, resulting in improved alignment accuracy and reasonable computational time, whilst the parameter for tie point limit ensured that the most reliable points detected-across overlapping photos-out of the 40,000 key point limit are retained and used for bundle adjustment and alignment refinement. The photo-alignment algorithm employed by Agisoft Metashape is based on the Structure from Motion (SfM) technique. It includes the Bundle Adjustment (BA) method formulated by Bill Triggs, Philip McLauchlan, Richard Hartley, and Andrew Fitzgibbon (Agisoft Metashape, 2024).

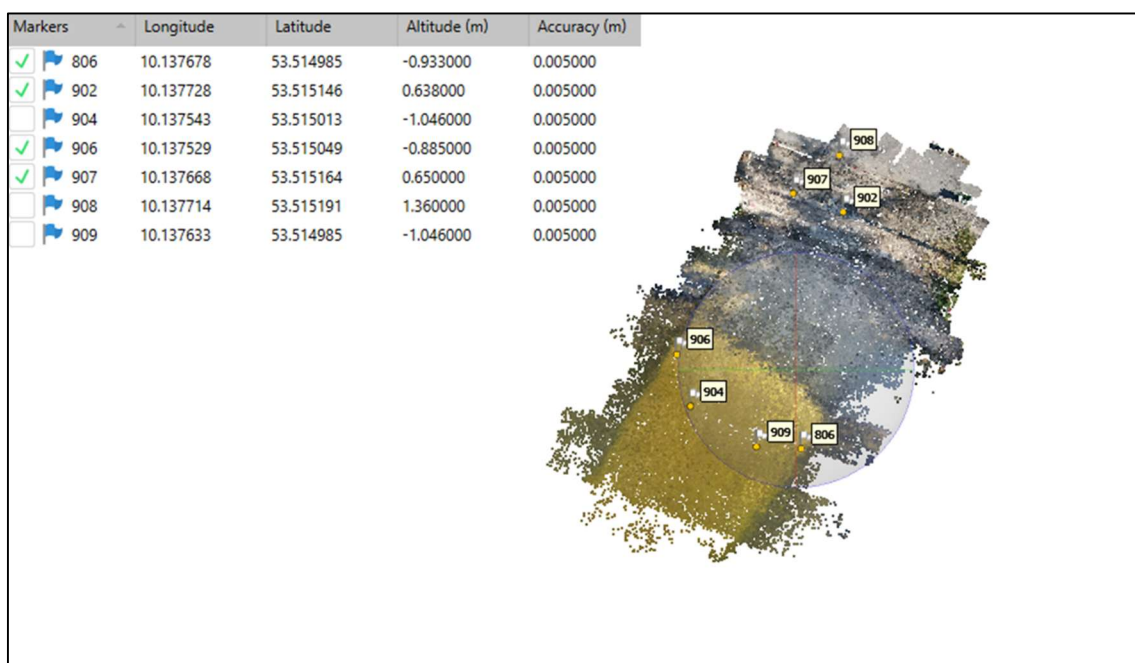


Figure 14: Import of GCP coordinates

Coordinates of GCPs -figure 14- were then imported for georeferencing and accurate orientation of aligned photos. Points 806, 902, 906 and 907 were used as control points during processing. GCPs 904 and 909 were used as checkpoints during the computation

of aerial imagery captured at a height of 5 m. GCPs 908, 904 and 909 were used as checkpoints in the computation of aerial imagery captured at heights 8 m and 10 m. The GCPs chosen as control points was done to achieve a rigorous geometrical spread of control points throughout the survey area. This ensured the creation of a polygonal network to minimize gross and systematic errors. Secondly, elevations of various points of interest are included for three-dimensional accuracy.

Having completed the alignment of aerial photos captured and importing GCP coordinates, the point cloud of the area of interest was computed. This was calculated using depth maps from detailed geometric data, ensuring higher accuracy and high quality to enhance the level of detail captured in the depth maps, critical for precise reconstructions and an aggressive depth filtering method to remove noise and ensure that the final point cloud is clean and usable.

Depth map computation was based on Gipuma, a novel and highly efficient method for Multiview stereo matching researched by (Galliani et al., n.d.). Gipuma enhances the PatchMatch algorithm by introducing a massively parallel approach that operates in Euclidean 3D scene space. This adaptation allows the aggregation of image similarities across multiple views, eliminating the need for epipolar rectification. The method leverages a new red-black propagation scheme tailored for GPU architectures, enabling simultaneous updates of alternate pixel groups and significantly improving computational speed. Additionally, the algorithm incorporates multiview matching through plane-induced homographies, utilizing overlapping views to enhance accuracy and robustness. Gipuma's strengths lie in its scalability, efficiency, and low memory requirements, making it well-suited for large-scale image datasets. The approach achieves linear scalability with image size and GPU thread count, processes ten 1.9-megapixel images in under three seconds on consumer-grade GPUs, and maintains a memory footprint of just four values per pixel. It delivers dense depth maps and point clouds without a fronto-parallel bias, making it ideal for industrial metrology, surveying, and computer graphics applications.

Experimental results on benchmark datasets like Danmarks Tekniske Universitet (DTU) Robot Image Dataset and Middlebury Multiview Stereo Dataset and Evaluation Benchmark demonstrate that Gipuma achieves state-of-the-art performance, offering high accuracy and completeness in 3D reconstruction tasks. The flexible framework allows users

to balance trade-offs between accuracy, completeness, and runtime efficiency depending on specific application needs (Galliani et al., n.d.). The parameters used can be observed in figure 15 below.

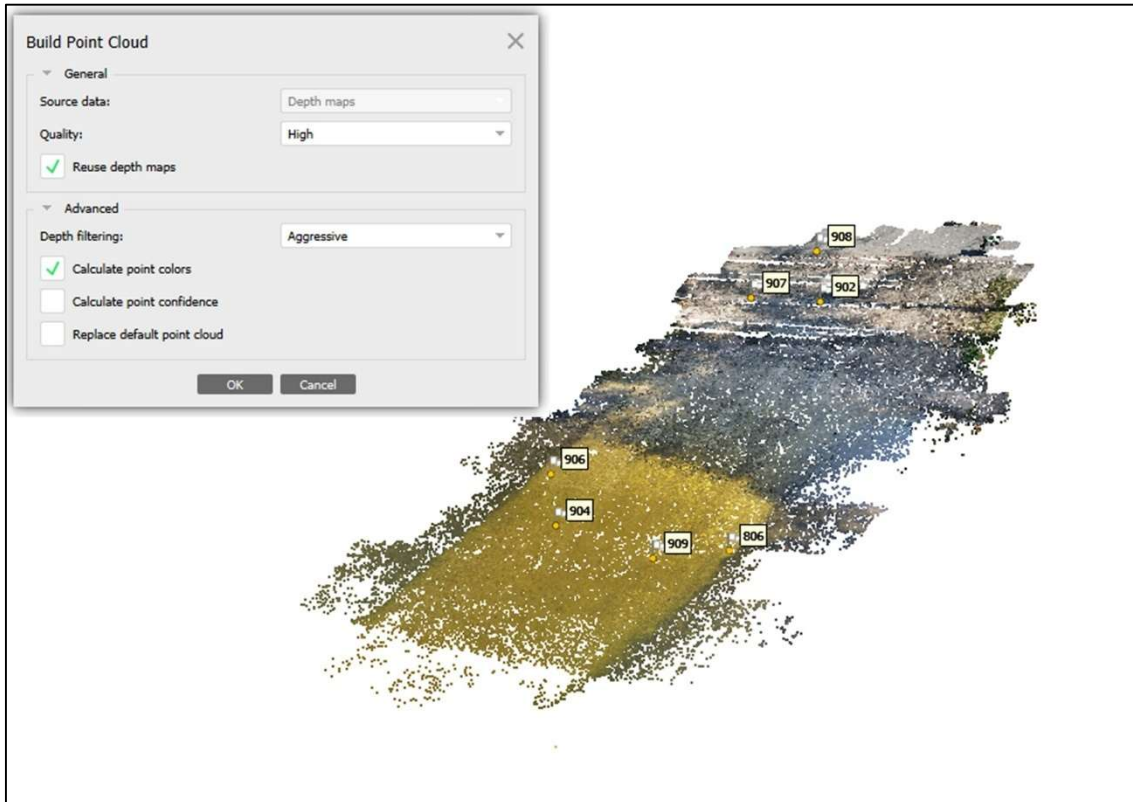


Figure 15: Computation of Point Cloud

A Digital Elevation Model (DEM) and an Orthomosaic were then generated. The DEM was generated - figure 16 – using the point cloud generated. The resolution of DEM was

fixed at 2.05 mm per pixel. An orthomosaic based on the DEM was computed - figure 17 - with a ground resolution of 1.02 mm per pixel.

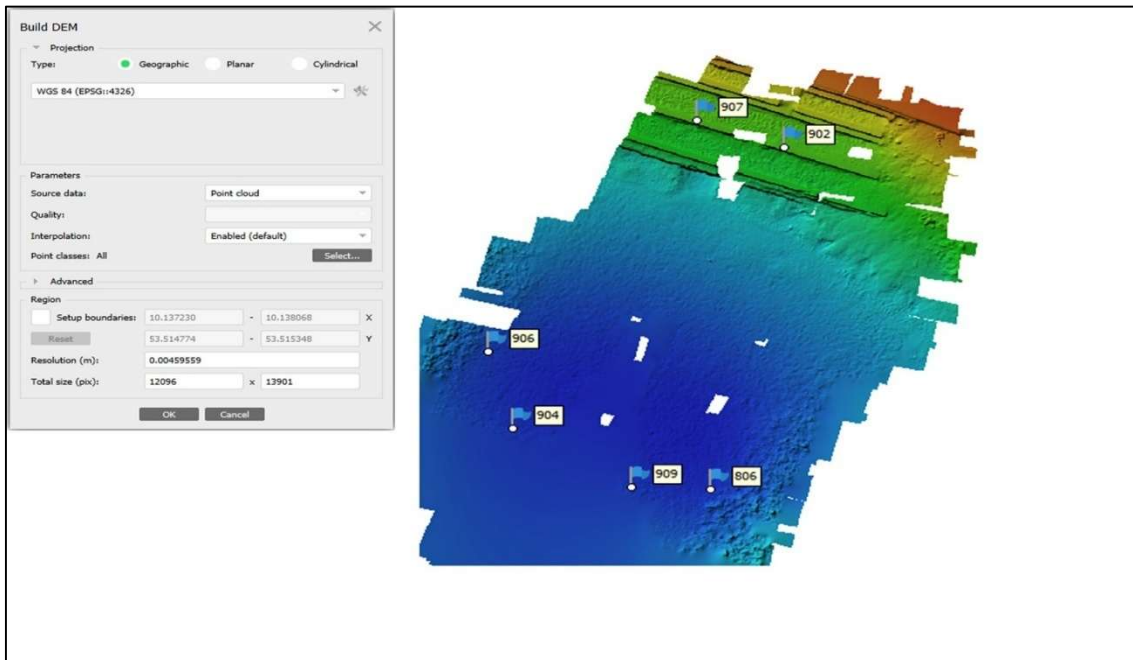


Figure 16: DEM computation

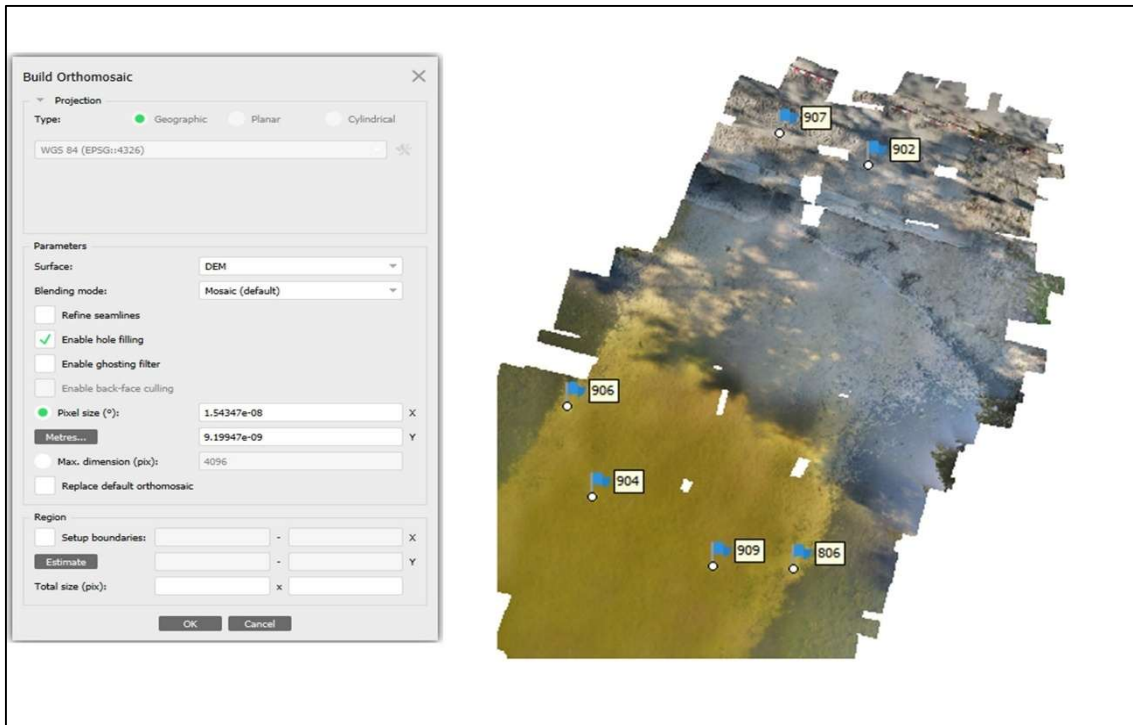


Figure 17: Orthomosaic computation

DEM computation was done based on the algorithm developed by (Pock et al., 2011). The algorithm termed TGV-Fusion is a method for fusing range images into high-quality digital surface models (DSMs) using Total Generalized Variation (TGV) regularization. This approach is tailored to generate 3D models of urban environments from highly overlapping aerial images. The focus is on creating a fully automated pipeline capable of handling the redundancy in input data, making it suitable for large-scale projects like virtual city modelling. The core innovation lies in the use of second-order TGV ( $TGV^2$ ) regularization, which is ideal for urban structures. Unlike traditional first-order smoothness methods,  $TGV^2$  supports piecewise affine surfaces, effectively modelling slanted surfaces like rooftops and building facades. The proposed fusion model integrates  $TGV^2$  with a robust Huber-L1 data term, ensuring accurate and noise-resistant results. To enhance computational efficiency, the authors developed a GPU-optimized primal-dual algorithm. This allows for fast processing and scalability, making it feasible to apply the method to large datasets. Experimental results on synthetic and real-world datasets demonstrate the model's robustness, accuracy, and suitability for urban 3D modelling.

The TGV-Fusion approach is particularly valuable for applications such as urban planning, infrastructure monitoring, and virtual city simulations. By addressing challenges like noise, redundancy, and computational efficiency, this method significantly advances the automation and accuracy of large-scale 3D reconstruction tasks (Pock et al., 2011).

The methodology outlined above was carried out in processing aerial imagery captured at the height of 5 m. The methodology was then repeated to process aerial imagery captured at heights of 8 m and 10 m.

Bathymetric data captured using Sonobot 1 was extracted as point data via its accompanying software, Neptus, as observed in figure 18.



Figure 18: Bathymetric data captured

According to the GPS data recorded during data capture, the pattern - figure 19 - of the altitude data showed a rise from 39.78 m to 39.94 m, which conformed to the depth readings recorded, which showed a minimum depth from 0 m to a maximum depth of 4.874 m as the Sonobot 1 moved from the edge of the water body close to land inwards. In other words, from the ultra-shallow to the shallow portion of the area under study.

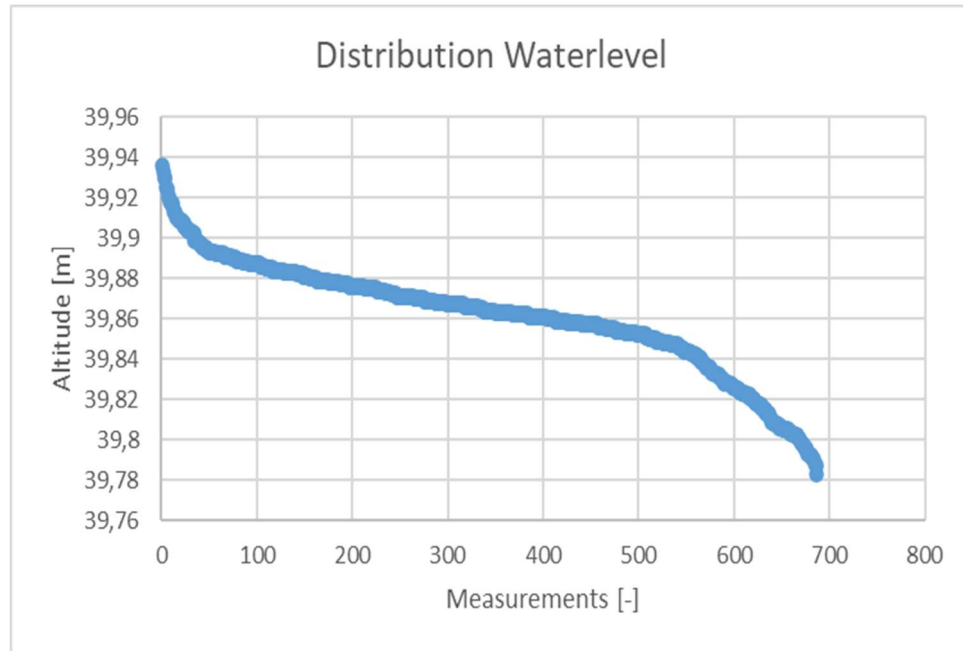


Figure 19: Pattern of altitude of GPS data recorded

In conducting the hydrographic survey using the Autonomous Surface Vehicle (ASV) Sonobot 1, which is equipped with a displacement hull, variations in factors such as speed, weight, and water depth can lead to measurable changes in the altitude recorded by the onboard GNSS. The GNSS system measured the altitude of the ASV relative to the ellipsoid, and these changes in altitude can be attributed to buoyancy effects, hydrodynamic forces, and environmental conditions. To understand these phenomena, an examination was conducted on how principles of physics, such as Archimedes' Principle and Bernoulli's Principle, influence the recorded altitude.

### Buoyancy and Archimedes' Principle

The displacement hull design of the Sonobot 1 ensures that it floats by displacing a volume of water equal to its weight, as dictated by Archimedes' Principle. This principle states that a floating object experiences an upward buoyant force equal to the weight of the water it displaces. The magnitude of this buoyant force depends on the density of the water and the volume displaced (Mott & Untener, 2015).

The ASV typically moves more slowly in shallow water to capture detailed and high-resolution bathymetric data. At slower speeds, the Sonobot 1's hull sits deeper in the water, displacing more volume to balance its weight. This increased water displacement causes the ASV to sit lower, resulting in lower GNSS altitude readings.

As the ASV transitions from shallow to deeper water, subtle environmental changes come into play. Water in deeper parts of a lake is often denser due to factors such as temperature stratification. Colder water at greater depths has higher density, meaning less volume needs to be displaced to achieve the same buoyant force. Consequently, the ASV floats slightly higher in deeper water, causing a gradual increase in the GNSS-recorded altitude. This effect, while minor, demonstrates the direct influence of buoyancy and the surrounding water's physical properties on the ASV's position (Fossen, 2011).

### **Hydrodynamic Forces and Bernoulli's Principle**

The effect of the ASV's speed becomes more prominent as it moves into deeper water, where faster speeds are often necessary to cover larger survey areas. This is where Bernoulli's Principle comes into play. Bernoulli's Principle states that as the speed of a fluid (in this case, water) increases, the pressure within the fluid decreases. When the Sonobot 1 moves at higher speeds, the water flowing under its hull creates a lower-pressure region, generating a hydrodynamic lift. This lift reduces the hull's contact with the water, causing the ASV to ride higher on the surface.

In shallow water, the Sonobot 1 operates at a reduced speed to enhance the accuracy of sonar and GNSS data collection. At these lower speeds, the hydrodynamic lift is negligible, and the ASV's hull remains in more significant contact with the water, leading to lower GNSS altitude readings. As the ASV accelerates in deeper water, the increased speed reduces drag and increases hydrodynamic lift. Combined with the denser water providing greater buoyant support, the ASV rises slightly in the water, leading to a higher GNSS-recorded altitude (Ardent Training, 2024).

### **Environmental Factors**

In addition to the physical principles of buoyancy and hydrodynamics, external environmental factors can influence GNSS altitude readings. For example, shallow water regions

are often more turbulent due to proximity to the lakebed, which can create waves and local disturbances. These disturbances may cause the ASV to bob slightly lower in the water. In contrast, deeper water is typically calmer, with reduced wave action and fewer external forces acting on the ASV, allowing it to maintain a more stable position and float slightly higher (Hodges et al., 2023).

Another factor to consider is the GNSS receiver's sensitivity and calibration. Minor variations in the ASV's tilt or position caused by movement and the GNSS system's interpretation of altitude relative to the ellipsoid can lead to small but noticeable changes in altitude measurements (Yastrebova et al., 2020).

### **How the Sonobot 1's Hull Design Plays a Role**

The Sonobot 1 features a displacement hull, which is optimized for stability and accuracy at slow speeds rather than high-speed planing. This design prioritizes consistent sonar and GNSS readings over rapid movement. The displacement hull ensures that the ASV remains steady, displacing water proportional to its weight, regardless of speed. However, as noted earlier, even with a displacement hull, the combined effects of buoyancy changes, hydrodynamic lift, and water density variations can still lead to measurable altitude differences when transitioning from shallow to deeper water (Puffin, n.d.).

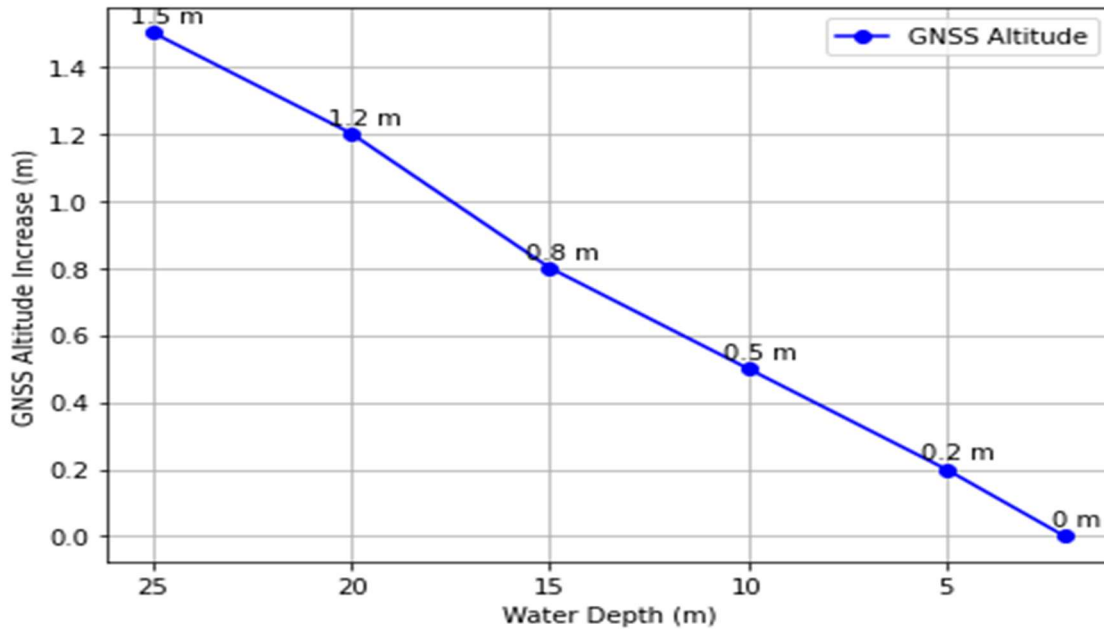


Figure 20: Effect of Depth on GNSS Altitude of ASV

An illustration of the effect of depth on the GNSS altitude of ASV is depicted in figure 20 above. With the combined effects of weight, speed, the hull design of the Sonobot 1 and environmental factors, as the ASV transitions from a depth of 5 m to 25 m hypothetically, the altitude recorded by the GNSS onboard the ASV will gradually rise or increase from 0 m to 1.5 m hypothetically.

A DEM using the bathymetric data captured was computed using the Inverse Distance Weighting (IDW) interpolation technique. IDW interpolation is a deterministic spatial interpolation method used to estimate unknown values at unsampled locations based on the values of surrounding sampled points. The fundamental assumption underlying IDW is that spatially closer points influence the interpolated value more than those farther away. This technique is widely applied in various fields, including environmental moni-

toring, geosciences, and terrain modelling, due to its simplicity and effectiveness in handling dense datasets. The interpolated value  $Z(x)$  - equation 2 - at an unknown location  $x$  is computed as a weighted average of known values at neighbouring locations:

$$Z(x) = \frac{\sum_{i=1}^N \omega_i Z(x_i)}{\sum_{i=1}^N \omega_i} \quad \text{equation 2}$$

where:

$Z(x_i)$ : known value at the  $i$ -th sampled location

$\omega_i$ : weight assigned to the  $i$ -th sampled location

$N$ : total number of neighbouring sampled points considered

The weight  $\omega_i$  - equation 3 - for each sampled point is inversely proportional to its distance from the target location, raised to a power parameter  $p$ , as expressed by the equation:

$$\omega_i = \frac{1}{d_i^p} \quad \text{equation 3}$$

Where:

$d_i$ : distance between the target location  $x$  and the sampled location  $x_i$

$p$ : power parameter, which determines the rate at which the influence of a sampled point decreases with distance.

The power parameter  $p$  plays a critical role in defining the influence of proximity on the interpolation results. Higher values of  $p$  increase the influence of closer points while diminishing the contribution of more distant points. Typically, a power value of  $p = 2$  (inverse square law) is commonly employed, reflecting a natural spatial decay influence. IDW often limits the interpolation process to a defined neighbourhood to optimise performance and ensure computational efficiency. This can be implemented by considering either a fixed radius around the target location or a predefined number of nearest sampled

points. Such constraints prevent distant or irrelevant points from influencing the interpolated value excessively.

The output of IDW is a smooth interpolated surface that mirrors the spatial distribution of the input data. However, in regions with sparse sampling or uneven distribution, the interpolated surface may exhibit "bullseye" patterns around individual points due to the overemphasis on their values (ESRI, 2024).

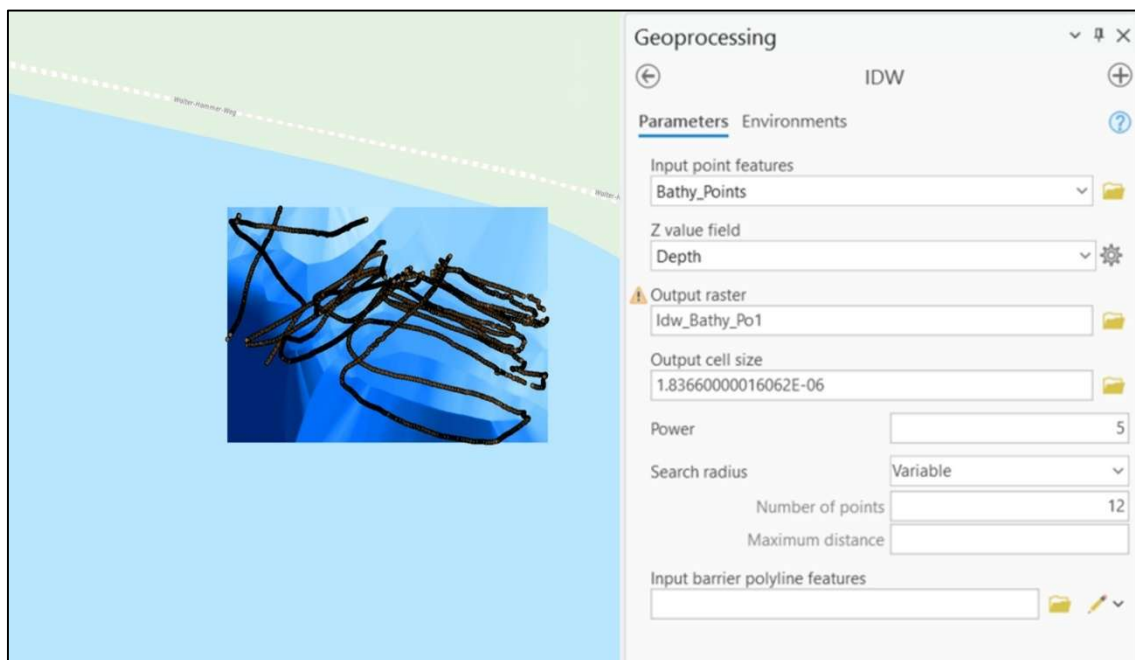


Figure 21: DEM computation from USV data

As mentioned earlier, using the depth value from the data obtained from sonobot 1 and a power value of 5, a DEM was computed with a resolution of 1.8336  $\mu\text{m}$ , as can be observed in image 21 above. An accuracy assessment of the output surface was done by performing an RMSE check. This was done by using the formula (equation 4):

$$\text{RMSE} = \sqrt{\frac{\sum_{i=1}^n (P_i - O_i)^2}{n}} \quad \text{equation 4}$$

Where:

$P_i$  = predicted or interpolated raster values

$O_i$  = measured or observed bathymetric point values

n = total number of selected points

Thirty per cent of the measured bathymetric points totalling 30 points were randomly selected for the computation of RMSE. This can be observed in figure 22. Interpolated values from the computed bathymetric surface were then extracted in QGIS using the tool add raster value to points and attached to the layer containing 30 per cent of the measured bathymetric data.

Computing the numerator of equation 4,  $\sum_{i=1}^n (P_i - O_i)^2$  the value of 0.1254 was obtained. Substituting this value in the remainder of the equation as shown below:

$$\text{RMSE} = \sqrt{\frac{0.1254}{30}} = 0.0647 \text{ m}$$

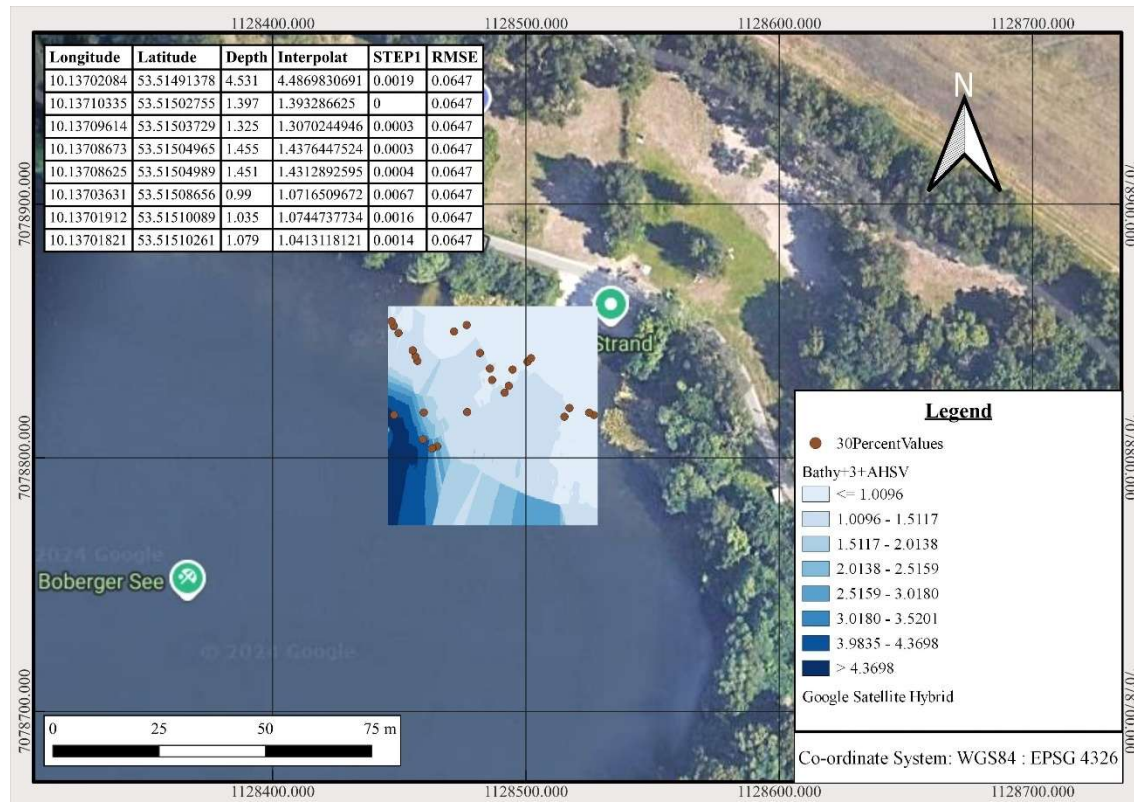


Figure 22: Computation of RMSE

## 4 Results And Discussion

### 4.1 UAV Computation Results

Using a total of 220 images aligned correctly, 240,052 generated tie points, computing the point cloud as depicted in image 23 below was done. The output shows the point cloud in terms of the elevation recorded for the site. A total of 85,532,810 points were obtained upon completion of the computation of the point cloud for the area of interest.

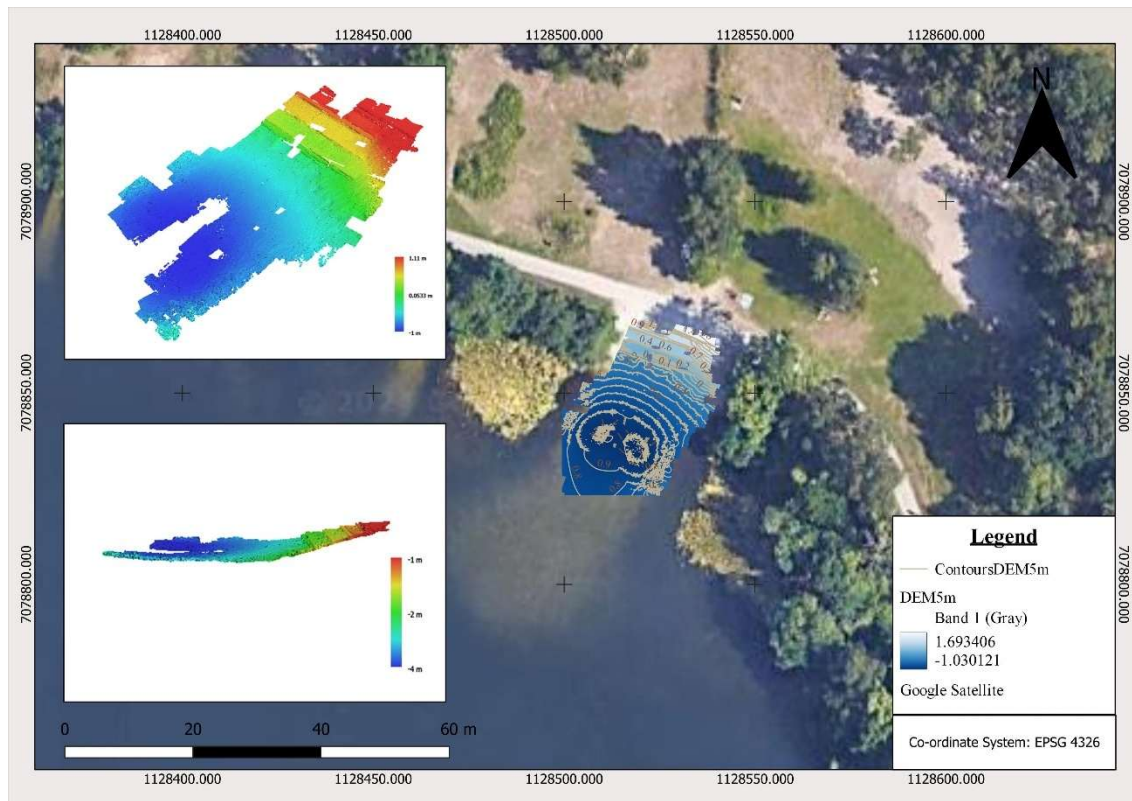


Figure 23: Point cloud computation output at UAV height 5 m

It can be observed from the side view of the point cloud computed no outliers were recorded. All points computed fell between the range of -1.03 m to 1.69 m, as can be noticed from the legend of the point cloud, which is shown in terms of elevation. It therefore implies that the parameters used in the computation of the images acquired by the UAV for the site of study were adequate. Due to the superfluous amount of data collected, as can be observed from figure 23 and 24, the DEM data computation output was masked to

narrow down the study to the relevant area of interest required, as can be observed from figure 24 before masking was applied and figure 25 after masking was applied below.



Figure 24: DEM before masking (UAV 5 m)



Figure 25: DEM after masking (UAV 5 m)

The Digital Elevation Model (DEM) – figures 24 and 25 - was generated from the 220 images all correctly aligned, 240,052 generated tie points, 7 GCPs (4 used as control points and 2 as checkpoints), a DEM of resolution 2.05 mm per pixel and a point density of 23.8 points per cm<sup>2</sup> was obtained. As can be observed from the images, small gaps can be seen in the final DEM computed.

An observation of the camera positions and overlap - figure 26 – showed a lack of images or non-existent overlap, leading to the lack of matching key points, causing the presence of these gaps or holes in the computed DEM.

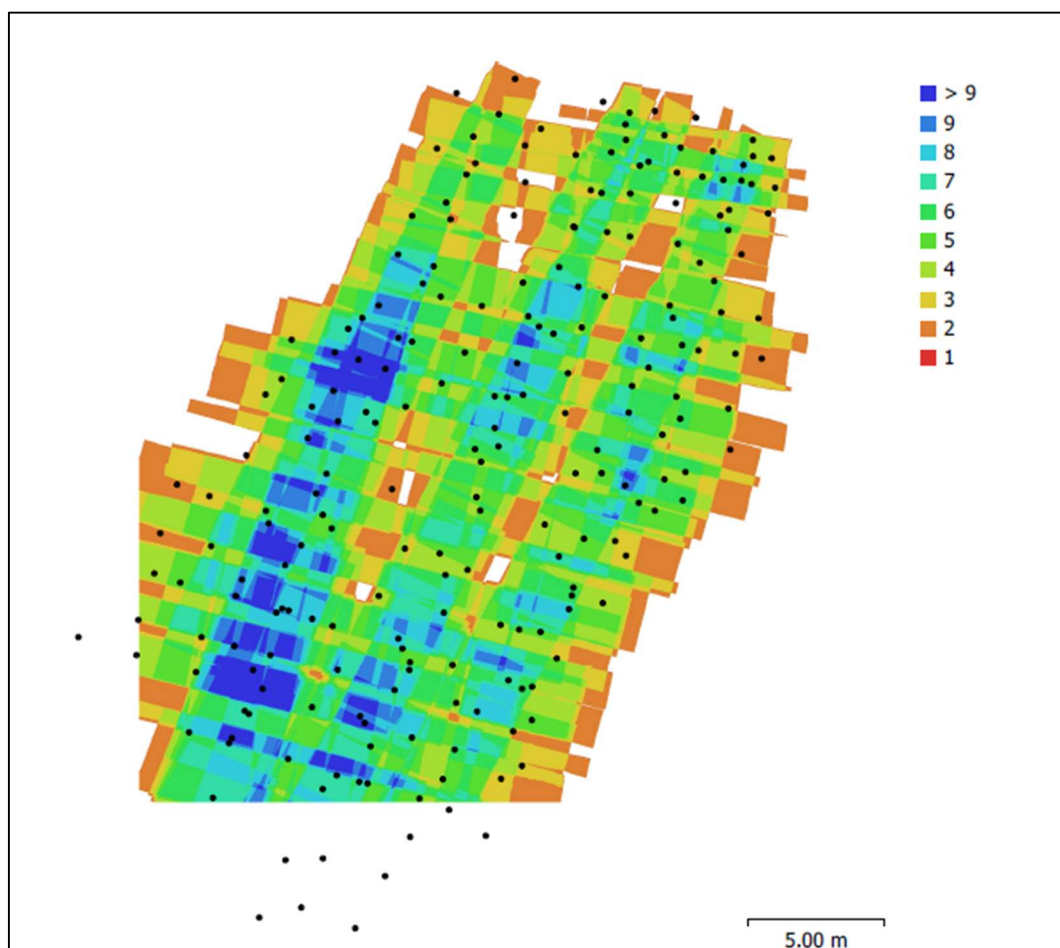


Figure 26: Camera positions and image overlap (UAV 5 m)

The Black dots indicate the estimated camera locations during data capture, and the legend indicates the extent of overlap. As can be observed, the overlap of images was low. Further evaluation of the camera positions during data capture revealed a total average

error of 3.21 m in the X, Y and Z directions. Errors computed with respect to x, y and z directions were 0.53 m, 2.18 m and 2.29 m, respectively. These can be visually observed from the error ellipses plotted from the camera positions in figure 27 below.

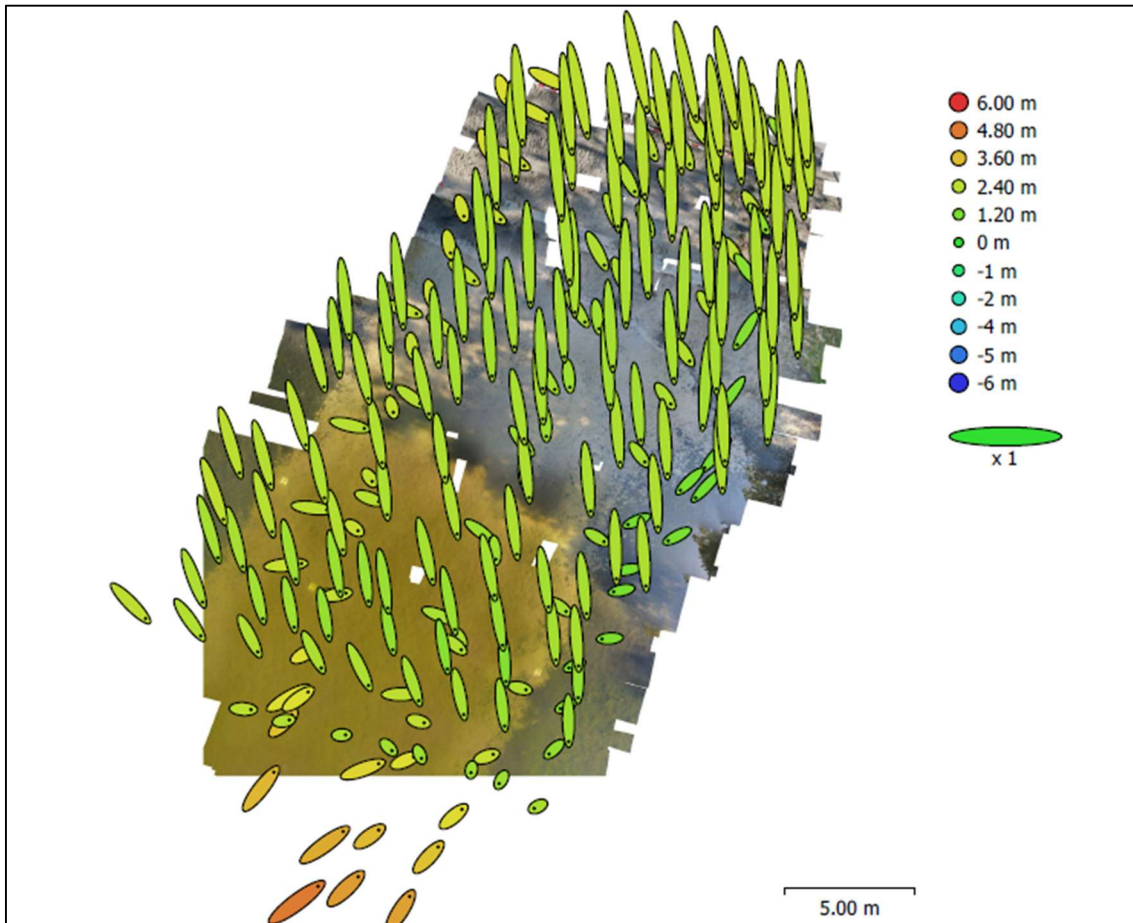


Figure 27: Camera locations and error estimates (UAV 5 m)

Z error is represented by the ellipse colour and X, Y errors are represented by the shape of the ellipse. Estimated camera locations are represented by the black dots. An assessment of GCP locations and their error estimates (figure 28) revealed that the Total RMSE of Control and Checkpoints were 21.045 cm and 42.07 cm, respectively, per tables 2 and 3 below.

Count	X error(cm)	Y error (cm)	Z error (cm)	XY error (cm)	Total (cm)
4	5.03857	20.4199	0.771797	21.0324	21.0465

Table 2: Control Points RMSE (UAV 5 m)

Count	X error(cm)	Y error (cm)	Z error (cm)	XY error (cm)	Total (cm)
2	39.7465	3.15461	13.431	39.8715	42.0729

Table 3: Check Points RMSE (UAV 5 m)

The X, Y Z errors of control and check points generated after computation can be observed in tables 4 and 5.

Label	X error(cm)	Y error (cm)	Z error (cm)	Total (cm)	Image (pix)
902	-6.94166	27.1947	-1.0624	28.0867	0.853
907	4.25228	-25.3463	1.11876	25.7248	0.662
906	5.32299	11.0013	-0.0371074	12.2215	0.900
806	-2.63555	-12.8405	-0.0315137	13.1083	0.950
<b>Total</b>	<b>5.03857</b>	<b>20.4199</b>	<b>0.771797</b>	<b>21.0465</b>	<b>0.868</b>

Table 4: Errors Control Points (UAV 5 m)

Label	X error(cm)	Y error (cm)	Z error (cm)	Total (cm)	Image (pix)
904	21.0396	3.66099	12.7364	24.8653	0.896
909	-52.124	-2.54957	14.0914	54.0553	1.052
<b>Total</b>	<b>39.7465</b>	<b>3.15461</b>	<b>13.431</b>	<b>42.0729</b>	<b>0.960</b>

Table 5: Errors Check Points (UAV 5 m)

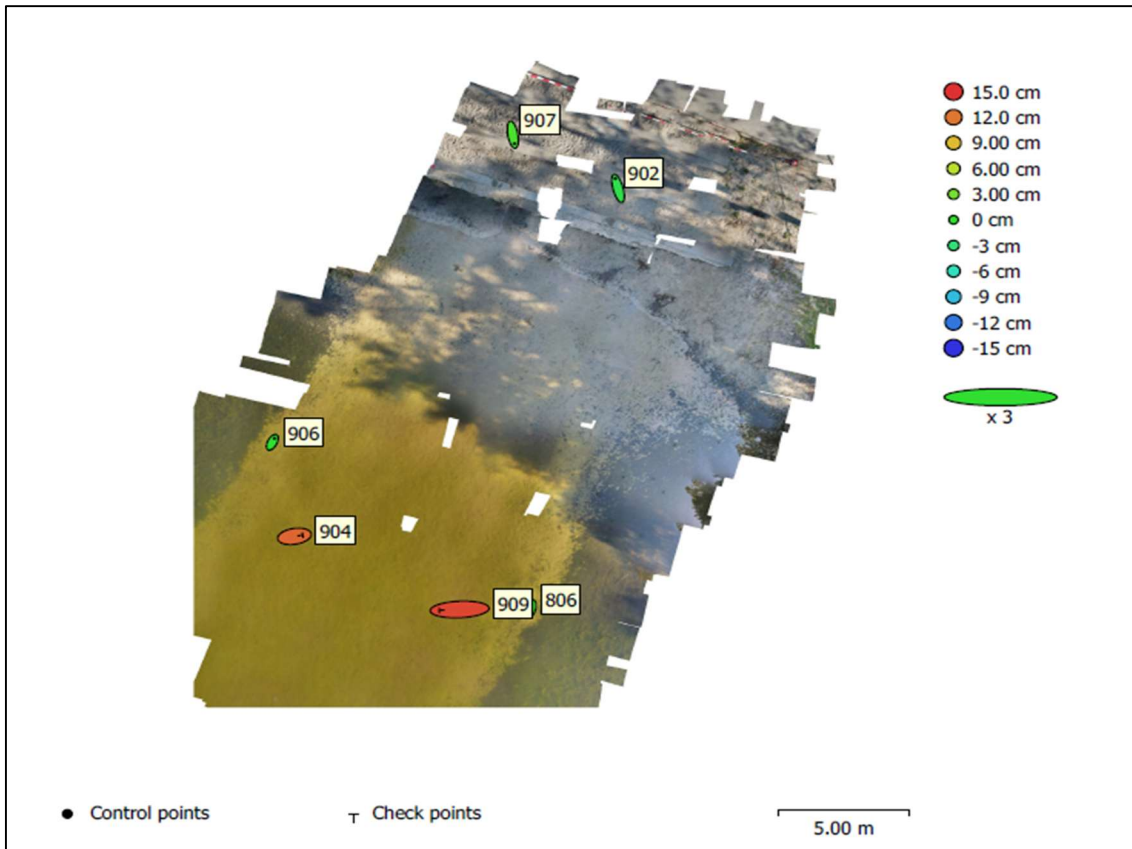


Figure 28: GCP Locations and error estimates at UAV height 5 m

A visual representation of the GCP locations and error estimates at the UAV height of 5 m is shown in figure 28. Z error is represented by ellipse colour. The X and Y errors are represented by ellipse shape. Estimated GCP locations are marked with a dot or crossing. A dot for control point(s) used and a crossing for checkpoint(s).

Similarly, the orthomosaic generated of the area surveyed before and after masking was applied can be observed in figures 29 and 30, respectively. Processing a total of 220 images, all images being correctly aligned, 240,052 generated tie points, 7 GCPs (4 used as control points and 3 as checkpoints), an orthomosaic of ground coverage  $459 \text{ m}^2$  and a ground resolution of 1.02 mm per pixel was obtained.



Figure 29: Computed Orthomosaic before masking (UAV 5 m)

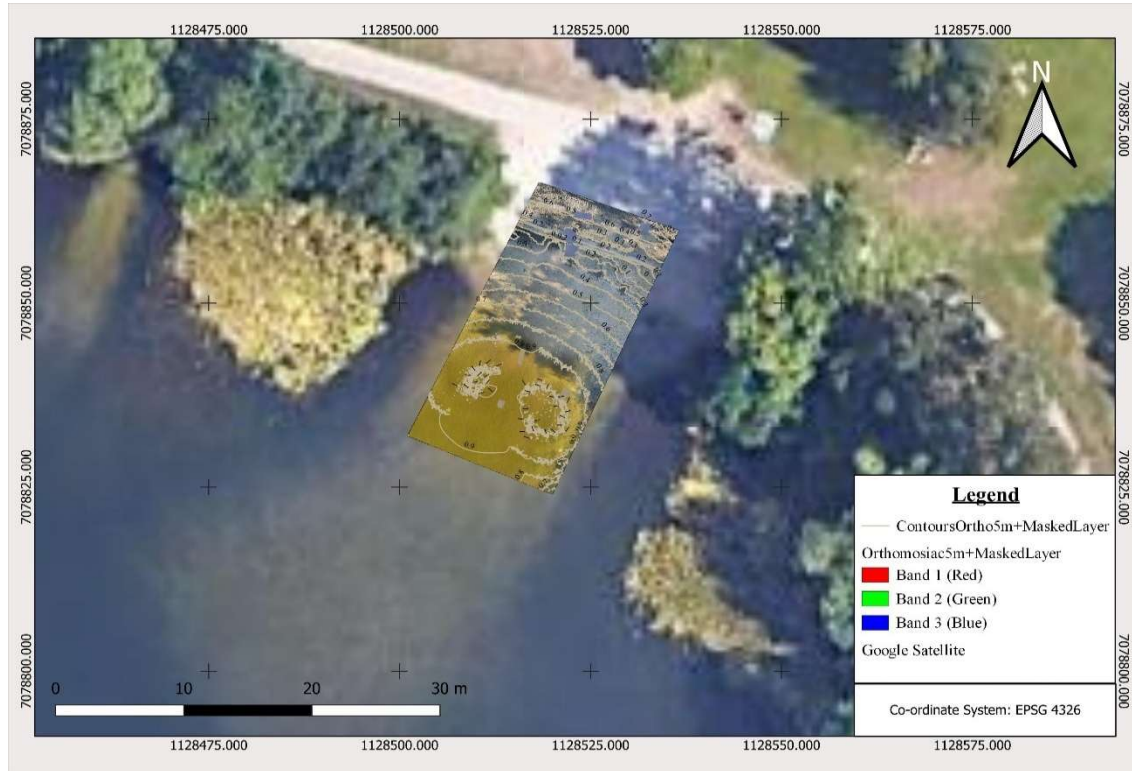


Figure 30: Computed Orthomosaic after masking (UAV 5 m)

As can be observed from the map, the same small gaps or holes in the final output data are present, similar to those present in the DEM output. The reasons for the presence of these gaps are the same as those cited for the gaps that were observed in the computed DEM output.

The computation of aerial data captured at the height of 8 meters involved processing 127 images, all correctly aligned, generating 95,751 tie points, and utilizing 4 GCPs as control points, while the remaining 3 GCPs were used as checkpoints. The point cloud output obtained, as can be observed from image 31 below, did not show the presence of any outliers. 25,631,829 points were obtained after computation. Points obtained were between the elevation range of -1 m to 1.47 m. The computation parameters used were the same as those used to compute aerial imagery captured at a height of 5 m.

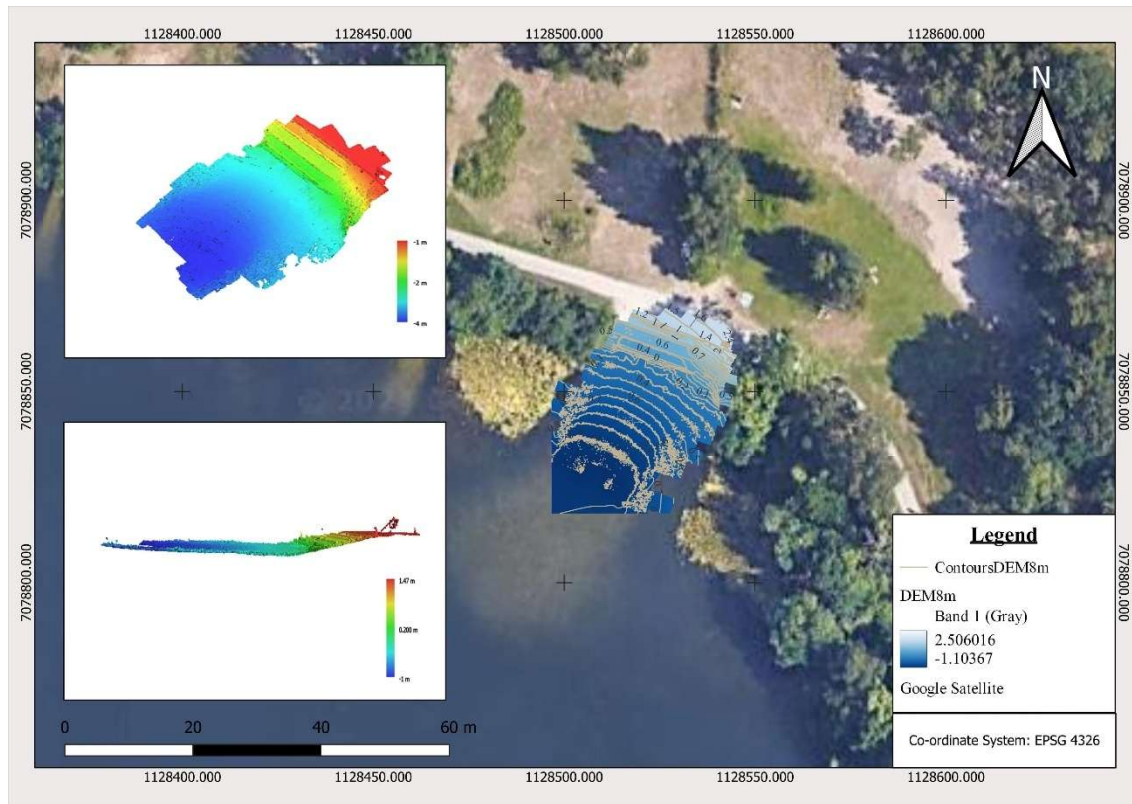


Figure 31: Point cloud computation output at UAV height 8 m

A DEM using the same input data was then computed and masked (figure 32) to narrow down the output to the area of interest. Computation parameters were the same as those used for aerial imagery captured at a height of 5 m. The resolution obtained was 4.73 mm per pixel, and the point density obtained was 4.76 points per cm<sup>2</sup>. Again, 127 correctly

aligned images, 95,751 generated tie points, 4 GCPs used as control points and 3 GCPs used as checkpoints were used in the computation of the DEM. The full output of the DEM obtained after computation can be seen in the appendix (figure 48).

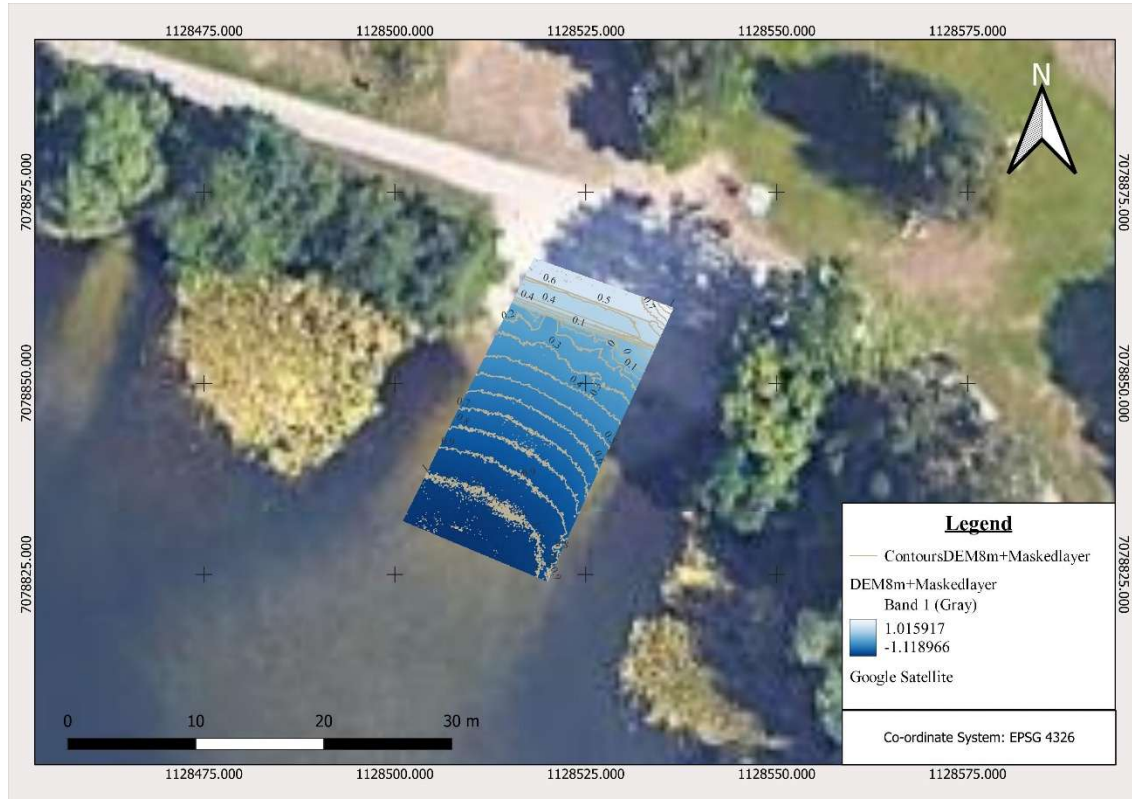


Figure 32: DEM after masking (UAV 8 m)

As can be observed from the DEM computed in figure 32, no gaps or holes are seen in the output. Figure 33 below shows the camera positions (indicated by black dots) and the degree of overlap. There was a high degree of overlap within the mid-section of the image, which corresponded to the area of interest. Additionally, no holes or gaps occurred in the final DEM output due to the significant overlap of images.

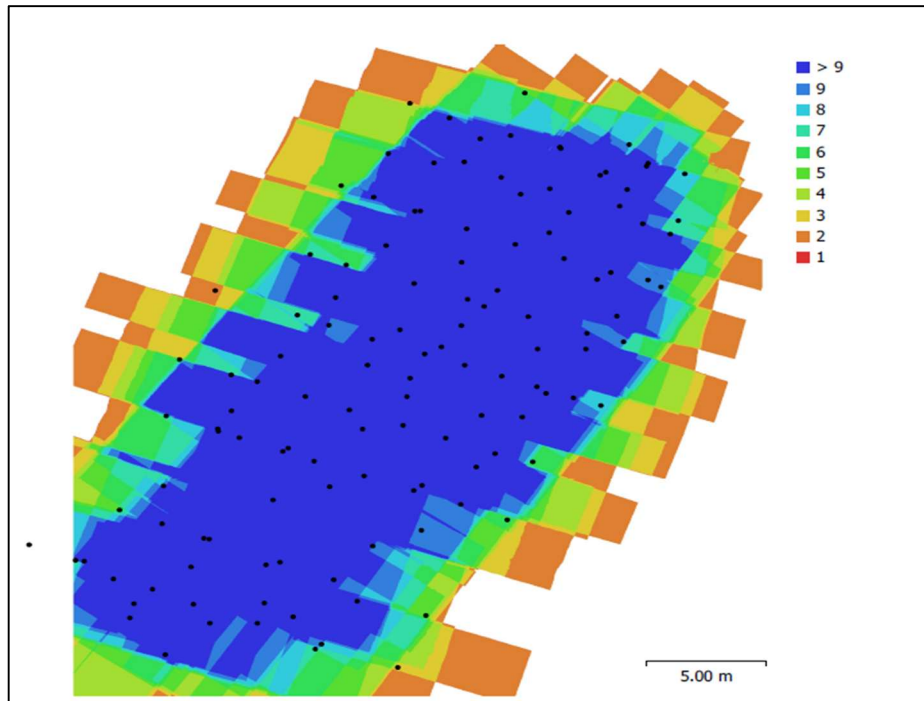


Figure 33: Camera positions and image overlap (UAV 8 m)

The total average camera location error estimated in the X, Y and Z directions was 3.10 m. Camera errors estimated in the X, Y and Z directions were 0.77 m, 1.77 m and 2.43 m, respectively. A visual representation of these errors can be observed in figure 34.

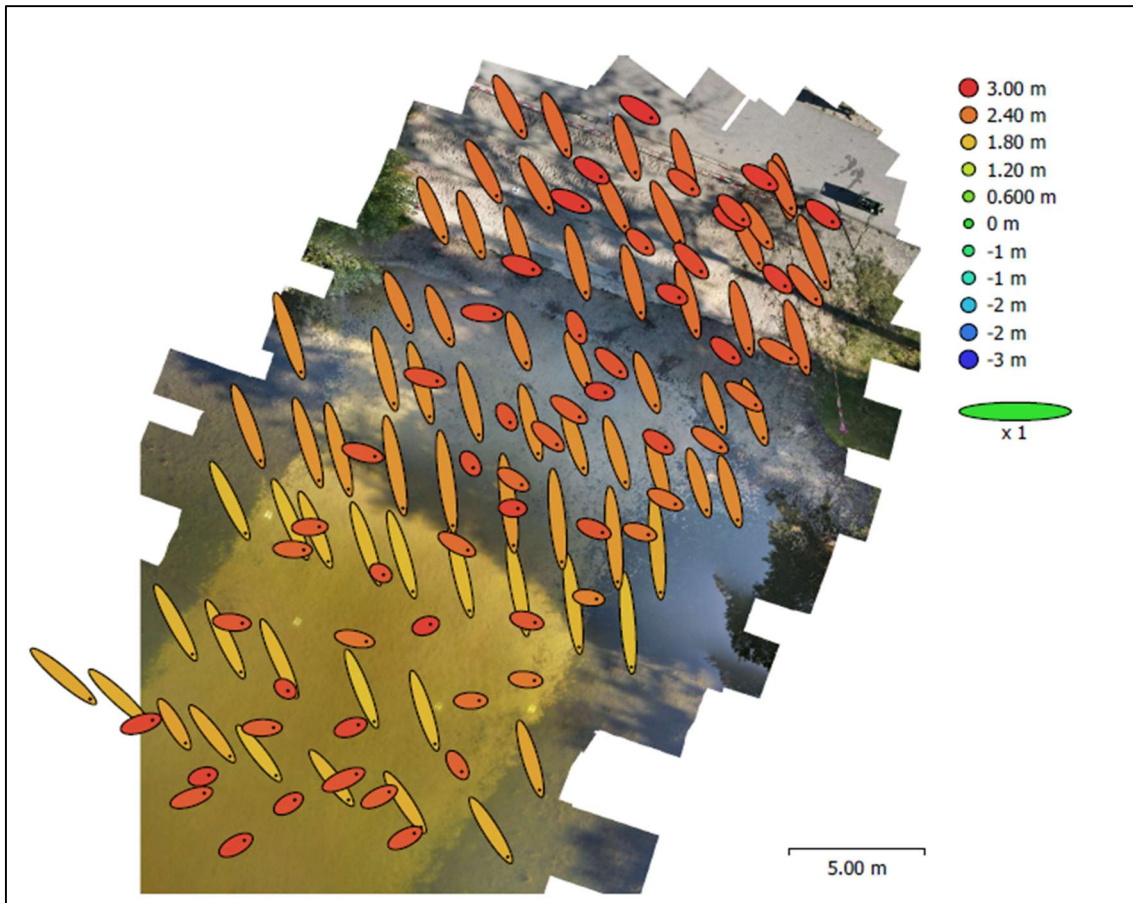


Figure 34: Camera locations and error estimates (UAV 8 m)

The Z error is represented by the ellipse colour, and the X, and Y errors are represented by the shape of the ellipse. The black dots represent estimated camera locations.

Assessing the GCP control and checkpoints used in computation revealed the following: in table 6, the total RMSE of the control points used in the direction of X, Y and Z was 21.72 cm.

Count	X error(cm)	Y error (cm)	Z error (cm)	XY error (cm)	Total (cm)
4	5.84253	20.9031	0.785393	21.7043	21.7185

Table 6: Control Points RMSE (UAV 8 m)

Table 7 indicates that the total RMSE of the GCP checkpoints used in the directions X, Y and Z was 52.12 cm.

Count	X error(cm)	Y error (cm)	Z error (cm)	XY error (cm)	Total (cm)
3	45.8417	24.5369	3.66973	51.9954	52.1247

Table 7: Check Points RMSE (UAV 8 m)

Label	X error(cm)	Y error (cm)	Z error (cm)	Total (cm)	Image (pix)
902	-7.15199	28.0169	0.747359	28.925	0.978
907	3.62793	-25.1664	-0.73268	25.4371	0.892
906	7.5066	11.3328	0.817015	13.6179	0.759
806	-3.98482	-14.1788	-0.839341	14.752	1.168
<b>Total</b>	<b>5.84253</b>	<b>20.9031</b>	<b>0.785393</b>	<b>21.7185</b>	<b>0.929</b>

Table 8: Errors Control Points (UAV 8 m)

Label	X error(cm)	Y error (cm)	Z error (cm)	Total (cm)	Image (pix)
908	54.385	-42.0632	5.87776	69.0042	0.638
904	21.7164	5.35521	2.27146	22.482	0.925
909	-53.6196	-2.86272	0.832549	53.7024	1.094
<b>Total</b>	<b>45.8417</b>	<b>24.5369</b>	<b>3.66973</b>	<b>52.1247</b>	<b>0.940</b>

Table 9: Errors Check Points (UAV 8 m)

Tables 8 and 9 show the X, Y, and Z direction errors of control and checkpoints used in the computation of the DEM.

Utilizing the same computation parameters as that of the aerial data captured at the height of 5 m and 127 images all correctly aligned, 95,751 generated tie points, 4 GCPs used as control points and 3 GCPs used as checkpoints, an orthomosaic (figure 35) was computed using aerial images captured at the height of 8 m. Output was masked to narrow it down to the area relevant to our study. The full extent of orthomosaic computed is included in the appendix, image 49.



Figure 35: Computed Orthomosaic after masking (UAV 8 m)

At the 10 m UAV height, 38 images were captured. These were all used as input data for the computation of the point cloud. All 38 images aligned correctly. 4 points of the GCPs measured on-site were used as control points, and the remaining 3 points were used as checkpoints. Point cloud output obtained comprised a total of 14,019,913 points. This was done using a total of 42,038 generated tie points. No outlying points were observed, as shown in figure 36 below. All points fell between the elevation range of -1 m to 1.39 m. The computation parameters used were the same as those used to compute aerial imagery captured at a height of 5 m.

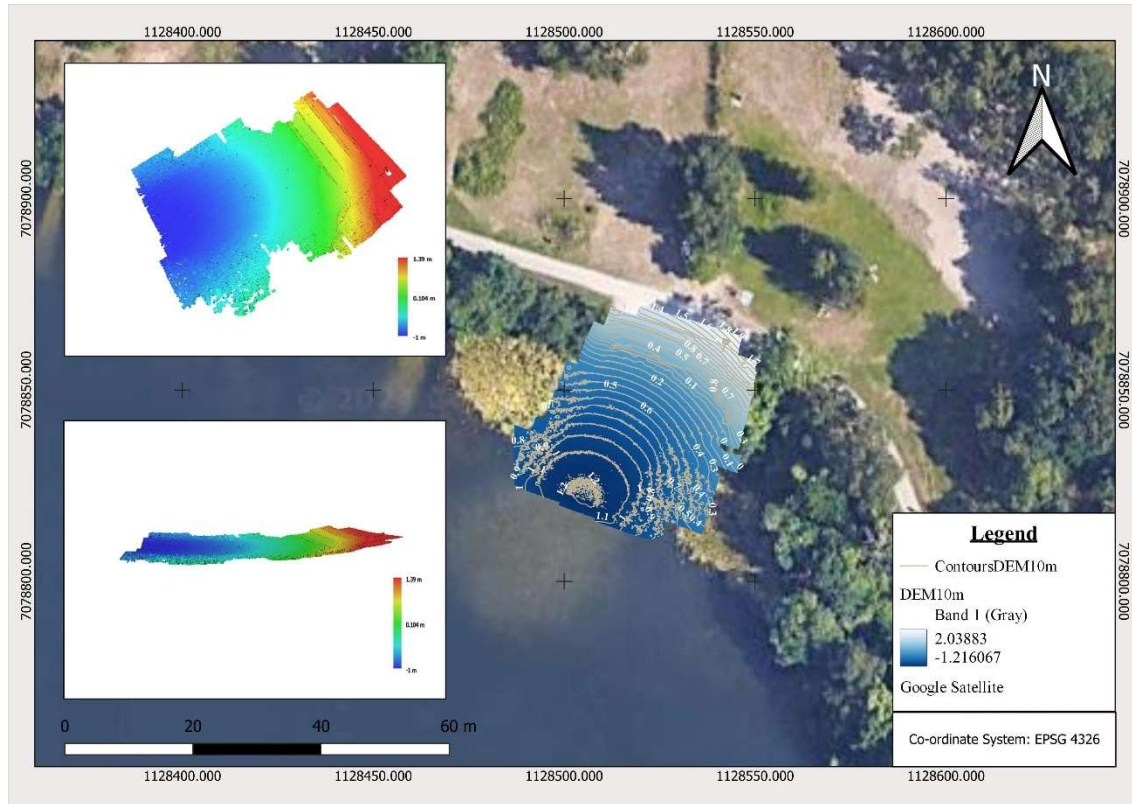


Figure 36: Point cloud computation output at UAV height 10 m

A DEM using the same input data was then computed and masked (figure 37) to narrow down the output to the area of interest. Computation parameters were the same as those used for aerial imagery captured at a height of 5 m. The resolution obtained was 7.46 mm per pixel, and the point density obtained was 1.80 points per cm<sup>2</sup>. Again, 38 images all correctly aligned, 42,038 generated tie points, 4 GCPs used as control points and 3 GCPs used as checkpoints were used in the computation of the DEM. The full output of the DEM obtained after computation can be seen in the appendix (figure 50).

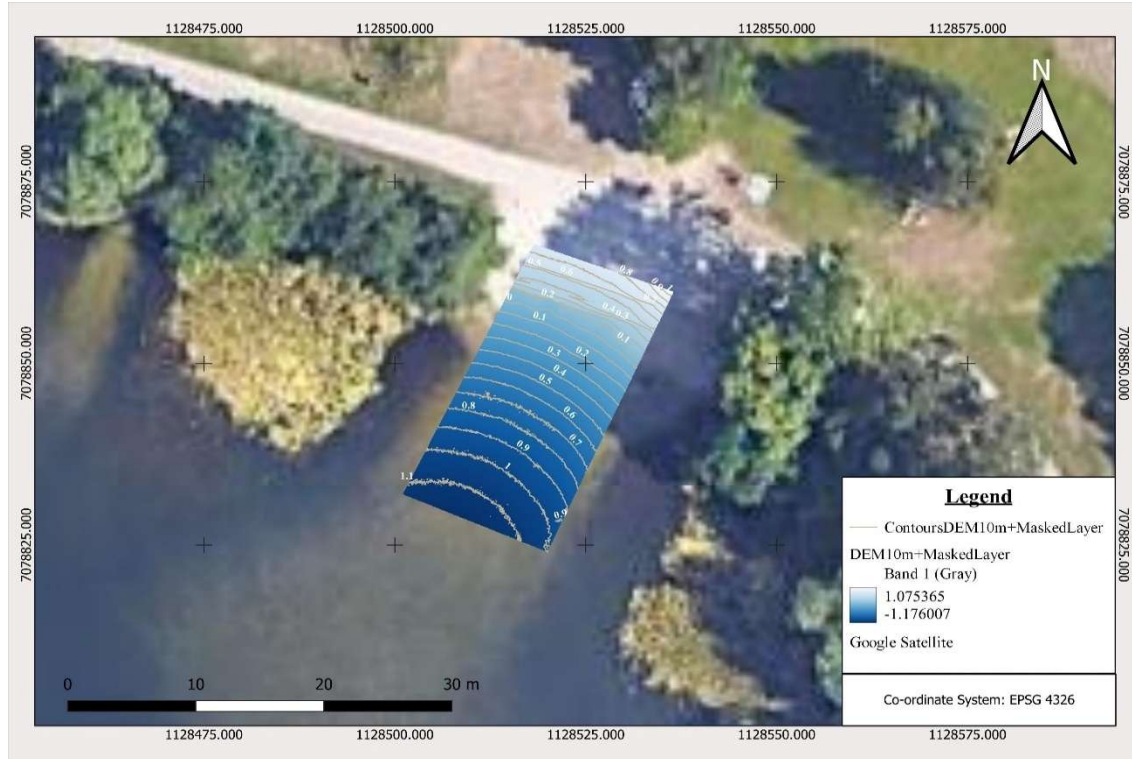


Figure 37: DEM after masking (UAV 10 m)

As can be observed from the DEM computed in figure 37, no gaps or holes are noticed in the output.

Assessing the GCP control and checkpoints used in computation revealed the following: in table 10, the total RMSE of the control points used in the direction of X, Y and Z was 28.07 cm.

Count	X error(cm)	Y error (cm)	Z error (cm)	XY error (cm)	Total (cm)
4	9.48199	26.3409	1.99689	27.9955	28.0667

Table 10: Control Points RMSE (UAV 10 m)

Table 11 indicates that the total RMSE of the GCP checkpoints used in the directions X, Y and Z was 49.87 cm.

Count	X error(cm)	Y error (cm)	Z error (cm)	XY error (cm)	Total (cm)
3	42.3928	26.1574	2.44237	49.8133	49.8731

Table 11: Check Points RMSE (UAV 10 m)

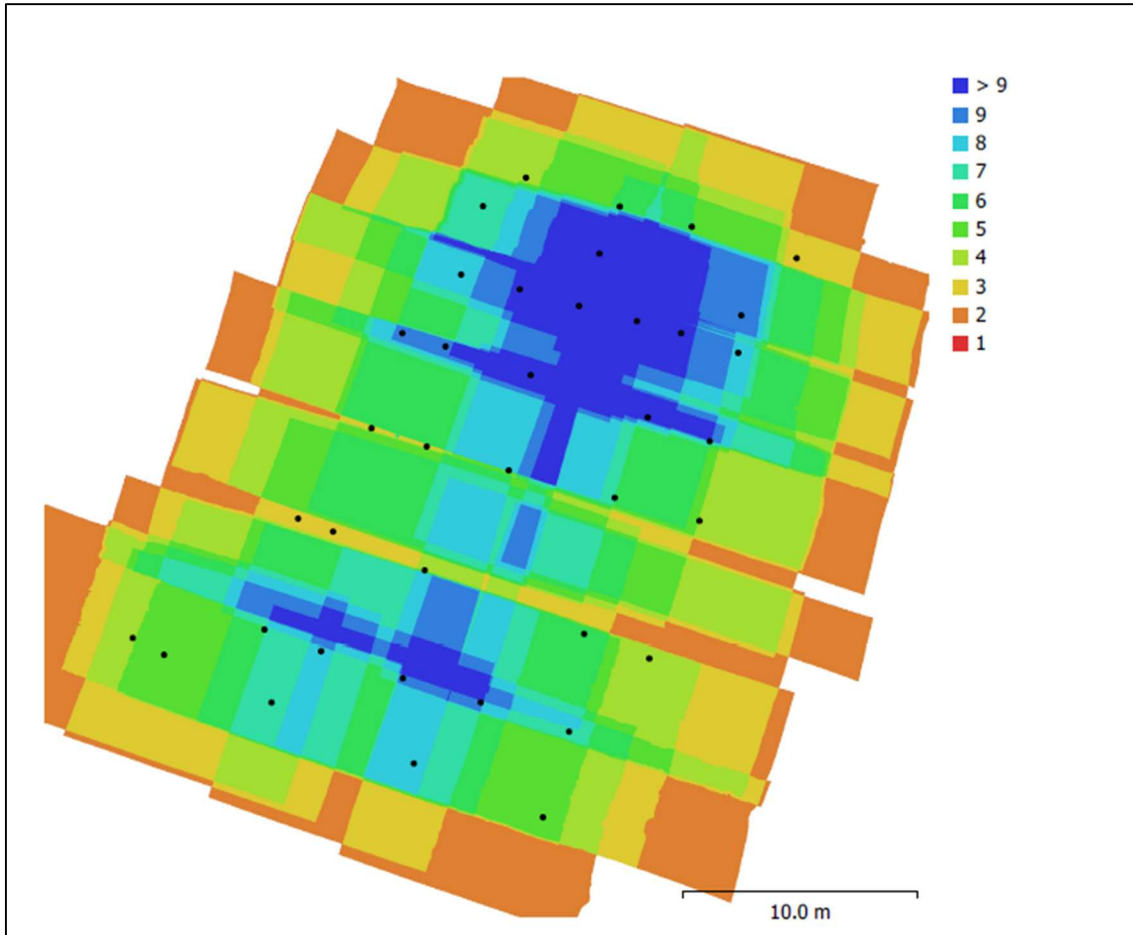


Figure 38: Camera positions and image overlap (UAV 10 m)

Image 38 shows the camera positions (indicated by black dots) and the degree of overlap. There was a significant decline in the degree of overlap within the mid-section of the image, which corresponds to the area of interest in the output obtained after the computation of aerial imagery captured at a height of 10 m compared to images captured at the UAV height of 8m. Although there was a decline in the overlap of images, no holes or gaps occurred in the final DEM output.

The total average camera location error estimated in the X, Y and Z directions was 5.92 m. Camera errors estimated in the X, Y and Z directions were 1.49 m, 1.70 m and 5.47 m, respectively. A visual representation of these errors can be observed in figure 39.

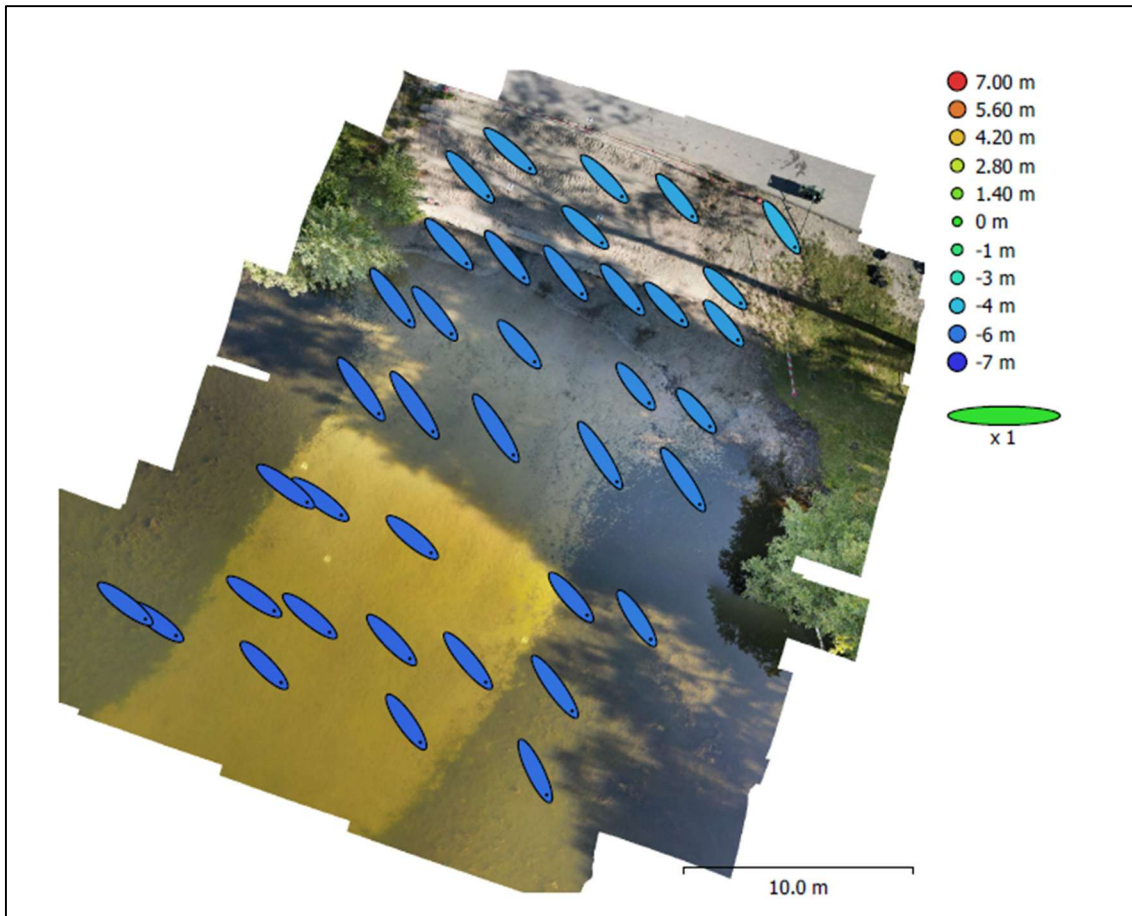


Figure 39: Camera locations and error estimates (UAV 10 m)

The Z error is represented by the ellipse colour and the X and Y errors are represented by the shape of the ellipse. The black dots represent estimated camera locations.

Tables 12 and 13 show the X, Y, and Z direction errors of control and checkpoints used in the computation of the DEM.

Label	X error(cm)	Y error (cm)	Z error (cm)	Total (cm)	Image (pix)
902	-9.1505	30.8804	1.60133	32.2474	1.307
907	-1.93794	-27.6498	-1.99274	27.7892	1.660
906	15.8071	21.3207	2.35888	26.6458	2.478
806	-4.72013	-24.5496	-1.9623	25.0761	1.574
<b>Total</b>	<b>9.48199</b>	<b>26.3409</b>	<b>1.99689</b>	<b>28.0667</b>	<b>1.706</b>

Table 12: Errors Control Points (UAV 10 m)

Label	X error(cm)	Y error (cm)	Z error (cm)	Total (cm)	Image (pix)
908	38.5609	-41.482	-3.14102	56.7236	0.550
904	23.9146	17.8186	-0.635507	29.8298	0.521
909	-57.7287	-3.79111	-2.76146	57.9189	0.850
<b>Total</b>	<b>42.3928</b>	<b>26.1574</b>	<b>2.44237</b>	<b>49.8731</b>	<b>0.717</b>

Table 13: Errors Check Points (UAV 10 m)

Utilizing the same computation parameters as that of the aerial data captured at the height of 5 m and 38 images all correctly aligned, 42,038 generated tie points, 4 GCPs used as control points and 3 GCPs used as checkpoints, an orthomosaic (figure 40) was computed using aerial images captured at the height of 10 m. Output was masked to narrow it down to the area relevant to our study. The full extent of orthomosaic computed is included in the appendix, image 51)



Figure 40: Computed Orthomosiac after masking (UAV 10 m)

## 4.2 Sonobot Data Computation Results

Data captured using the Sonobot 1 was computed using QGIS and ArcGIS Pro. Utilizing the interpolation technique IDW a DEM was produced. The resolution of the DEM obtained was  $1.8366 \mu\text{m}$ . DEM computed can be observed in figure 41 below.

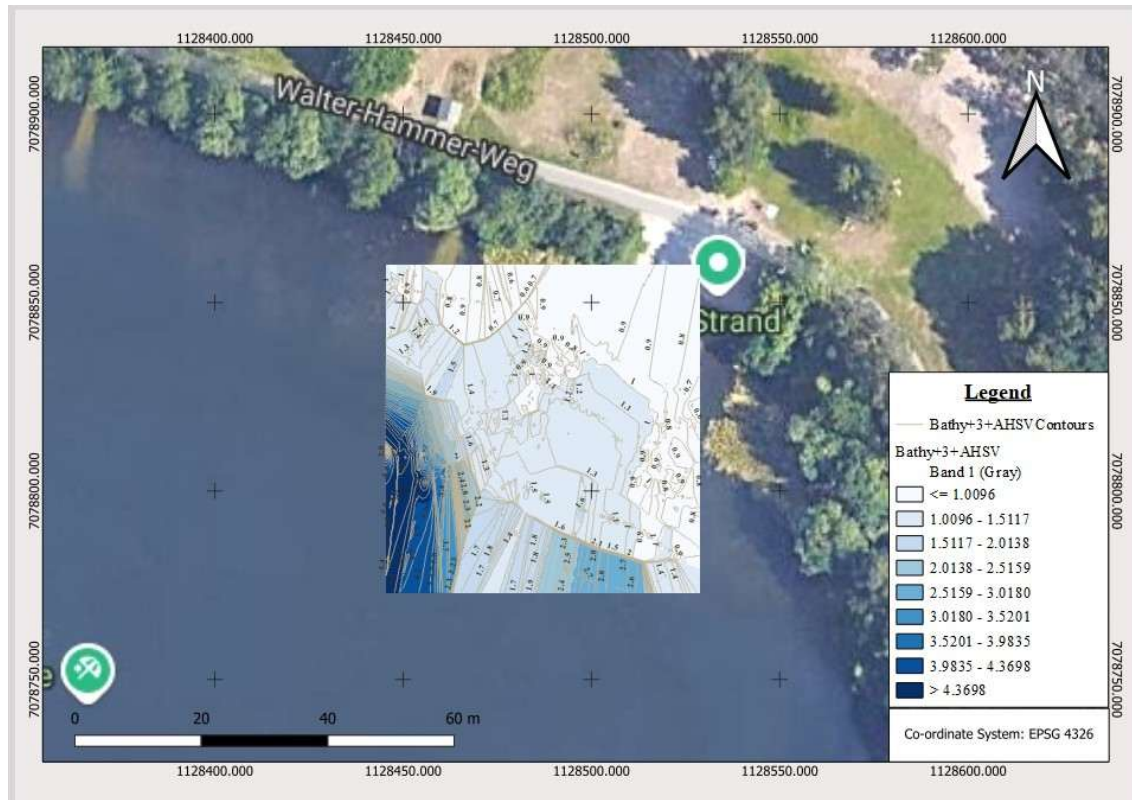


Figure 41: DEM computed from ASV data

DEM was computed from a total of 12,013 points with a minimum vertical RMSE of 0.74 m and a maximum RMSE of 1.05m. Referring to figure 42 below, 10,000 plus points had the GNSS fix type mode AA assigned to them. 200 plus points had the GNSS fix type mode FF assigned to them, whilst 600 plus points had the GNSS fix type mode RR assigned to them.

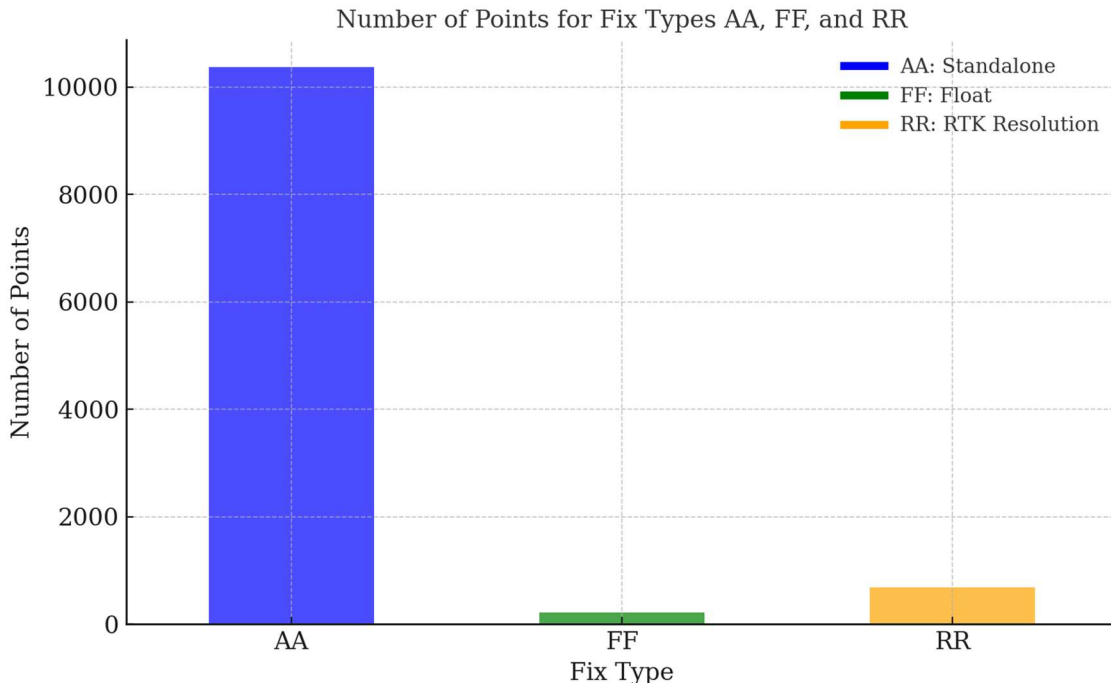


Figure 42: Plot of points measured and recorded with their corresponding GNSS mode of measurement

The GNSS or GPS measurement was assessed using Horizontal Dilution of Precision (HDOP) values and the number of satellites tracked during the survey. HDOP is a critical metric in GNSS (Global Navigation Satellite System) that measures how satellite geometry influences the accuracy of horizontal position calculations. It specifically assesses the precision of latitude and longitude measurements and serves as a key indicator of the reliability of GNSS data. HDOP is derived from the geometric arrangement of satellites visible to the GNSS receiver. When satellites are well-distributed across the sky, HDOP values are lower, resulting in higher positional accuracy. Conversely, clustered or poorly positioned satellites lead to higher HDOP values, reflecting reduced accuracy. This makes HDOP a vital consideration in applications requiring precise location data. HDOP values directly relate to the positional error and are dimensionless. Lower values indicate better accuracy:

- Low HDOP (< 2): High accuracy due to well-distributed satellites.
- Moderate HDOP (2 - 5): Acceptable accuracy for most general applications.

- High HDOP (>5): Poor accuracy caused by inadequate satellite geometry, such as satellites being clustered or positioned near the horizon.

Satellites evenly spread across the sky enhance accuracy. Tight clusters or alignment degrade it. Physical barriers like buildings, trees, or mountains can block satellite signals, disrupting geometry and increasing HDOP.

With observed HDOP values ranging from 0.9 - 1.4 and the number of satellites tracked during the survey from as low as 6 to as high as 13, GNSS measurements were fairly reliable. This can be observed from the collage of images in image 43 below.

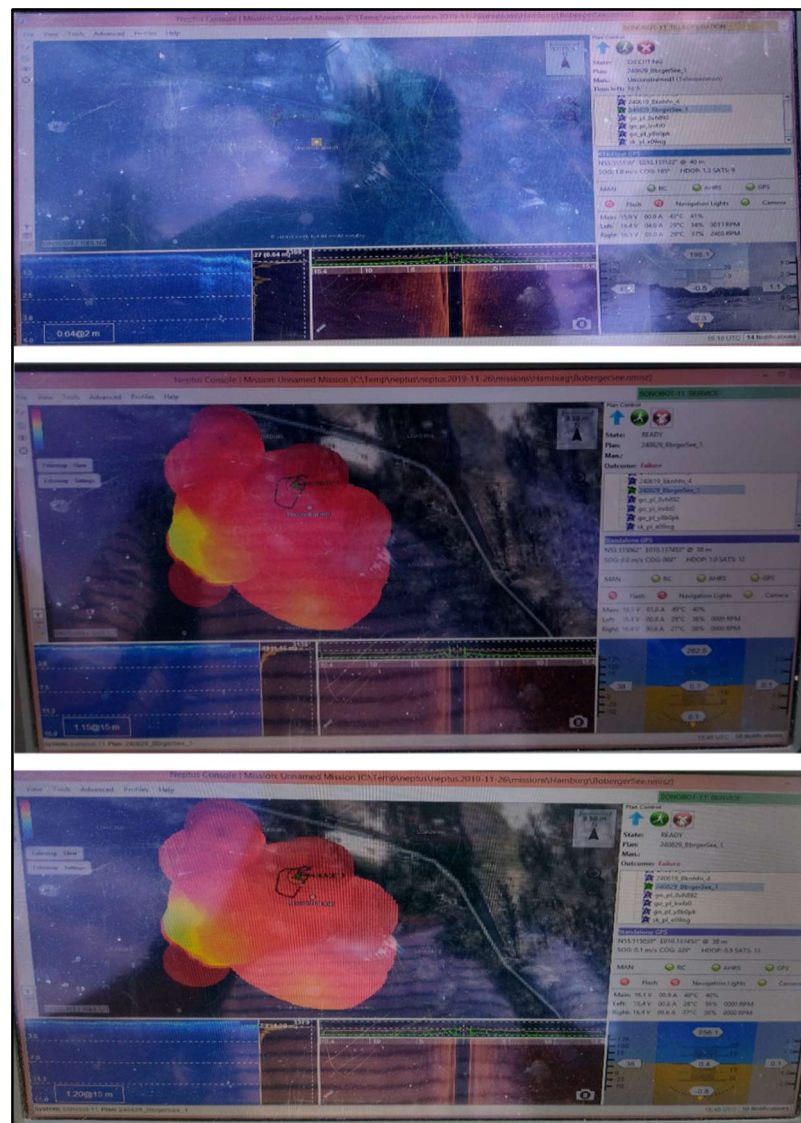


Figure 43: GNSS assessment during the survey

The acceptability of the stated RMSEs is attributed to the depth range surveyed (0.50 – 4.85 meters), indicating that the measured values exhibited minimal deviations and that only minor errors were inherent in the measurements. Again, the RMSE value computed using equation 4 gave a value of 0.0647 m, indicating that the DEM computed from the measured bathymetric data demonstrates a high level of precision, with an average error of 6.47 cm, as indicated by the RMSE value of 0.0647 m. This level of accuracy is well within acceptable error tolerances for most bathymetric computations. Such precision ensures that the DEM reliably represents the underwater topography of the study area, meeting the stringent requirements necessary for scientific and practical applications in the field of hydrography.

Furthermore, the results validate the effectiveness of the methodologies and algorithms employed in the study. Techniques such as Inverse Distance Weighting (IDW) interpolation for processing hydroacoustic data proved robust and reliable. This method enabled the creation of the bathymetry from data obtained using the ASV of the shallow portion of the area under study with minimal error.

The output obtained was masked (figure 44) to narrow down to the area of interest and allow for integration with the DEM obtained from UAV data processed.

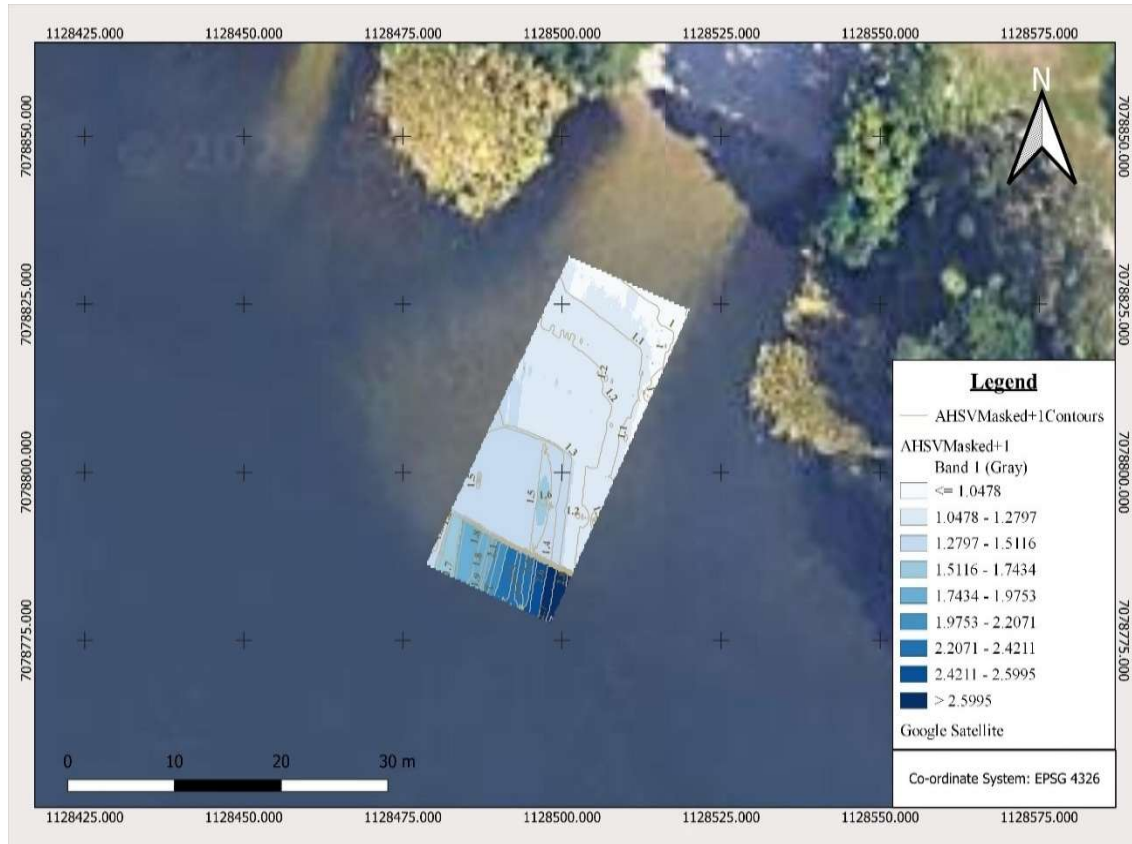


Figure 44: ASV DEM after masking

### 4.3 Fusion of DEMs

Creating a seamless DBM using the DEM datasets computed from the aerial imagery acquired using the UAV and bathymetric data acquired using the Sonobot involved utilizing the mosaic to raster tool found in ArcGIS Pro. The DEM computed from aerial imagery acquired at the height of 8 m was chosen to be integrated with the DEM obtained from bathymetric data acquired using the ASV. The choice of this dataset was primarily due to the high degree of overlap extent compared to that of DEMs computed from aerial imagery acquired at heights of 5 m and 10 m. Secondly, the RMSE values obtained for the Z direction of control points and checkpoints were better when compared to data acquired at a height of 5 m and close to data acquired at 10 m.

The Mosaic to Raster operation in ArcGIS Pro combines multiple raster datasets into a single cohesive raster. When the Mosaic Operator Mean is applied, the tool resolves overlapping areas by calculating the average value of all overlapping raster cells. For each

pixel in the output raster, the mean operator computes the average of the corresponding pixel values from all input rasters that overlap at that location. For example, if three overlapping rasters have pixel values of 10, 20, and 30 at a specific location, the resulting pixel value in the output raster will be 20, which is the average of the three values. In regions where only one raster contributes, its value is directly assigned to the output raster. When handling NoData values, these are excluded from the mean calculation. For instance, if two overlapping rasters have pixel values of 10 and 20, and a third overlapping raster has a NoData value, the average is calculated as 15, which is the mean of the two valid values. However, if all overlapping rasters have NoData values at a given location, the output pixel will also be assigned NoData. This method is particularly useful in creating a seamless raster surface, as it smooths transitions in overlapping areas, mitigates outliers, and provides a balanced representation of input data (ESRI, 2025)

Using UAV DEM having a 4.73 mm per pixel resolution and 1.8336  $\mu\text{m}$  pixel resolution for DEM obtained from the Sonobot dataset, a seamless bathymetric model (figure 45) was computed. The elevation range was between  $> 0.60$  m to  $\leq 2.48$  m. The average pixel resolution of the final DEM computed was  $0.953985 \mu\text{m} \times -0.939568 \mu\text{m}$ . This was overlaid with a generated contour of interval 0.05 m, as displayed in figure 46.

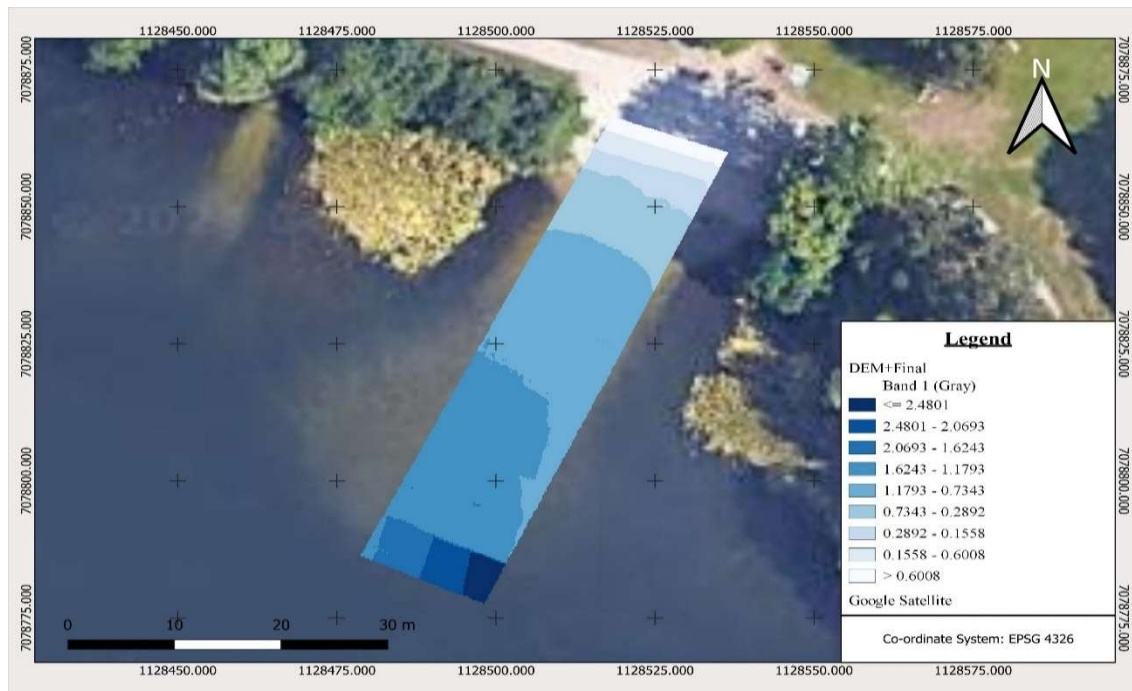


Figure 45: Final DEM ASV dataset integrated with UAV dataset

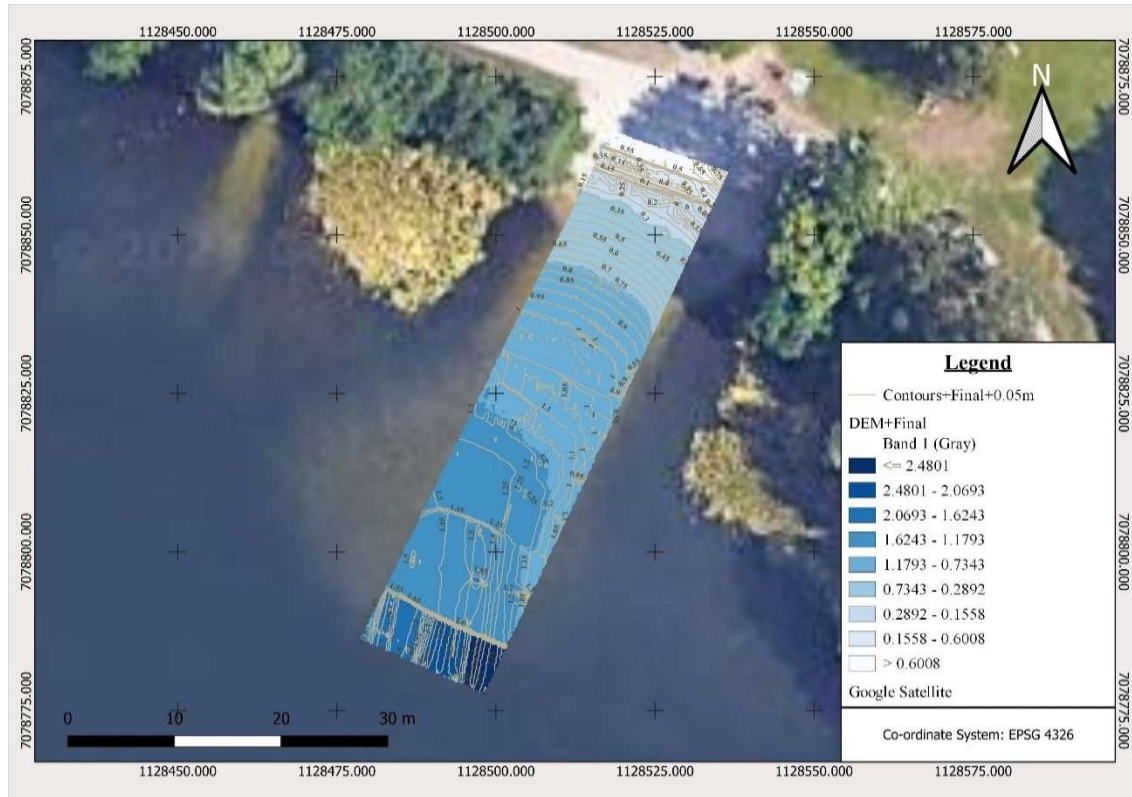


Figure 46: Final DEM ASV dataset integrated with UAV dataset with contours

A 3D visual output of the merged DEMs was generated, as displayed in figure 47. This buttressed the contour heights and depth of the created DBM. Depth increased inwards from the edge (ultra-shallow) of the water close to land towards the inner portions of the water (shallow), as can be observed. This was an accurate representation of the bathymetry of the area under study confirm the methodology utilized is acceptable.

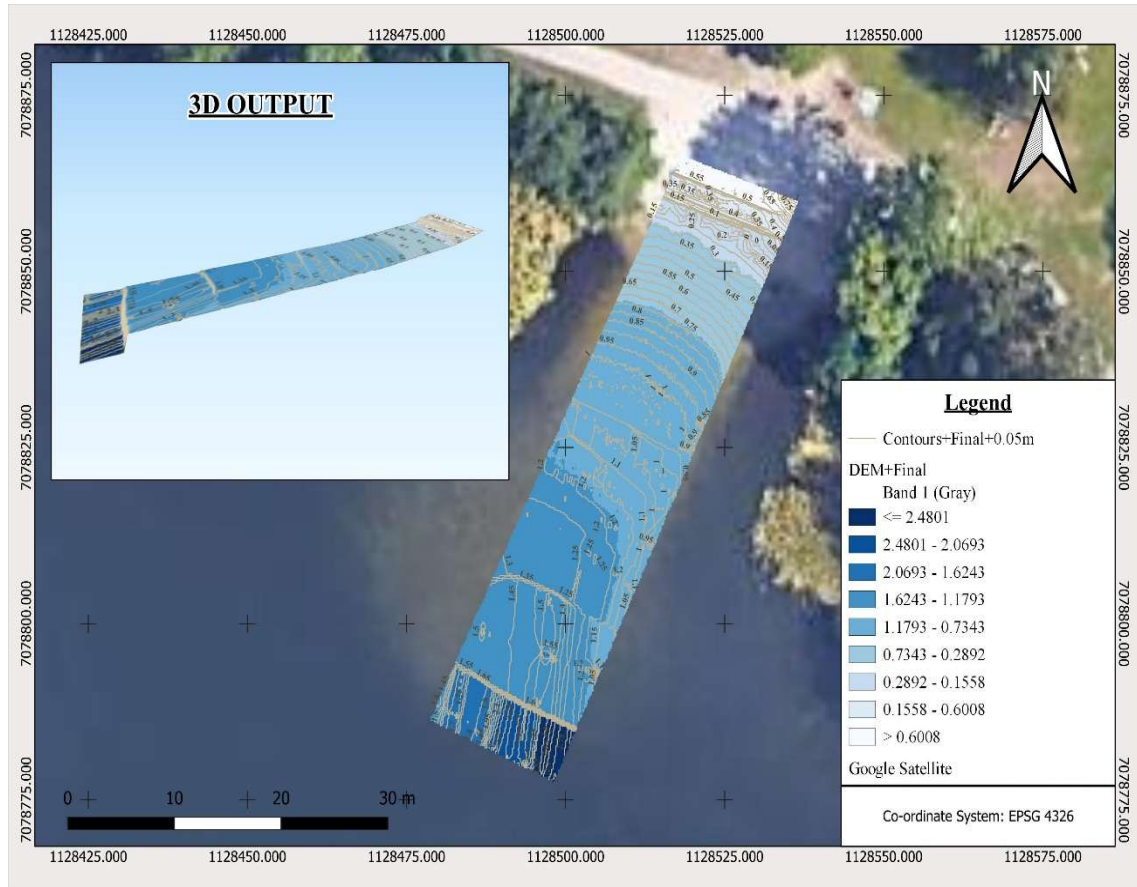


Figure 47: 3D Visualized Output of Final DEM ASV dataset integrated with UAV

## 4.4 Conclusion

The research successfully demonstrates the feasibility of creating a seamless Digital Bathymetric Model (DBM) by integrating data from hydroacoustic and photogrammetric sources, specifically in challenging shallow and ultra-shallow water environments. Using advanced tools such as the Autonomous Hydrographic Survey Vehicle (Sonobot 1) and UAV-based photogrammetry, this study has highlighted the strengths and compatibility of these technologies in addressing the complexities associated with underwater topography.

Key outcomes of the study include the generation of high-resolution Digital Elevation Models (DEMs) with minimal errors and gaps despite the inherent challenges of data collection in dynamic and shallow aquatic settings. Using robust algorithms, such as Gipuma for point cloud generation and TGV-Fusion for DEM computation, ensured precision and efficiency in data processing. Furthermore, the study validated the methodology by achieving an RMSE value of 0.0647 m, reflecting high accuracy and reliability in the fused bathymetric model.

The hydrographic survey conducted with the Autonomous Surface Vehicle (ASV) Sonobot 1, equipped with a displacement hull, demonstrated that variations in speed, weight, and water depth influenced the altitude recorded by the onboard GNSS. These changes are attributed to buoyancy effects, hydrodynamic forces, and environmental conditions governed by Archimedes' and Bernoulli's principles. Archimedes' Principle explains that the ASV floats by displacing water equal to its weight; in shallow water, slower speeds result in greater water displacement, causing the ASV to sit lower and record lower GNSS altitude readings. In deeper water, denser water requires less displacement for the same buoyant force, allowing the ASV to float higher and increasing GNSS altitude. Bernoulli's Principle highlights that as the ASV moves faster in deeper water, reduced pressure beneath the hull generates hydrodynamic lift, raising the ASV's altitude. In contrast, slower speeds in shallow water minimize hydrodynamic lift, causing the ASV to remain deeper in the water. Environmental factors, such as turbulence in shallow water and calmer conditions in deeper water, also affect stability and GNSS measurements. Despite

the stability provided by the Sonobot 1's displacement hull, the combined effects of buoyancy, hydrodynamic lift, and water density variations result in measurable altitude differences as the ASV transitions from shallow to deep water.

Again, the unaccounted ship movements of the ASV may have led to the variations in GNSS readings. Unaccounted ship movements during hydrographic surveys using the Autonomous Surface Vehicle (ASV) Sonobot 1 can significantly impact the accuracy of GNSS measurements, leading to errors in both altitude and geographic position. These movements, including roll, pitch, yaw, heave, sway, and surge, disrupt the stability and orientation of the GNSS antenna, causing misalignment and positional inaccuracies. Vertical motions such as heave can distort altitude readings, as the GNSS system may interpret these changes as variations in the ASV's true position relative to the ellipsoid, leading to errors in in-depth calculations. Additionally, sway and surge cause lateral displacement of the ASV, resulting in incorrect georeferencing of sonar data and potential distortions in the bathymetric model. Rapid changes in orientation due to roll or pitch may degrade GNSS signal quality, introducing multipath errors or intermittent data loss. These errors can accumulate over time, compounding the inaccuracies in the survey results.

Integrating aerial photogrammetry with hydroacoustic data proved effective, providing a comprehensive representation of shallow and ultra-shallow regions. This seamless fusion enhances the precision of underwater topographic mapping and sets a foundation for further research into improving cost-efficiency and operational scalability in hydrographic surveying.

Aerial imagery data offers a significant advantage over UAVs equipped with LiDAR due to its cost-effectiveness and ability to capture rich visual details. High-resolution cameras used for aerial imagery are generally less expensive to acquire, operate, and maintain than LiDAR sensors, making it an affordable solution for large-scale mapping projects. Aerial imagery provides detailed visual information, including RGB data, critical for creating orthophotos, textured 3D models, and land-use classifications. Unlike LiDAR, which excels in capturing accurate geometric data, aerial imagery delivers rich colour and texture, making it ideal for urban planning, vegetation analysis, and infrastructure monitoring applications. Additionally, cameras are lighter than LiDAR sensors, enabling UAVs equipped with aerial imagery systems to have longer flight times and greater operational

range. Photogrammetry software can process aerial imagery to generate dense point clouds, 3D models, and Digital Elevation Models (DEMs), offering versatile post-processing options. While LiDAR is preferred for penetrating dense vegetation, mapping complex terrains, or operating in low-light conditions, aerial imagery remains optimal for cost-efficient, visually detailed, and adaptable applications.

In conclusion, this research underscores the potential of combining innovative technologies and methodologies to address the limitations of traditional bathymetric surveys. It offers valuable insights and tools for applications in environmental management, urban planning, and infrastructure development, particularly in hard-to-survey areas. Future studies could build on these findings by exploring additional datasets and refining computational techniques to enhance accuracy and operational efficiency further.

## 4.5 Recommendation

This study highlights the potential of integrating photogrammetric and hydroacoustic datasets for creating seamless Digital Bathymetric Models (DBMs) in challenging shallow and ultra-shallow environments. Several recommendations are proposed for future research and applications to build on these findings.

Firstly, data fusion techniques must be optimized to enhance the integration of photogrammetric and hydroacoustic datasets. Employing advanced methods, such as machine learning-based fusion or adaptive algorithms, can address gaps or inconsistencies in the combined models, resulting in higher precision and reliability. Additionally, expanding the methodology to diverse environments, such as turbid coastal zones or vegetated inland water bodies, can help validate the robustness and adaptability of the approach under different conditions.

The improvement of sensor capabilities is also essential. Incorporating higher-resolution sensors and more advanced technologies, such as multi-beam echo sounders or LiDAR systems, can significantly enhance the accuracy and applicability of bathymetric surveys. Furthermore, refining accuracy assessment techniques by employing additional validation metrics or independent datasets can bolster confidence in the results, ensuring their reliability for critical applications.

Automation and scalability are crucial for large-scale implementation. Automating key processes such as data pre-processing, alignment, and interpolation will reduce manual intervention, making the workflow more efficient and scalable for real-time or extensive surveys. Similarly, incorporating alternative data sources, such as satellite-derived bathymetry or multispectral imagery, can complement the existing methodology, particularly in regions where UAVs or hydrographic survey vehicles face operational challenges.

Practical applications and policy considerations should also be explored. Governments and organizations can leverage the seamless DBMs generated through this approach for environmental conservation, navigation planning, and infrastructure development. These models can provide critical data for effective management and monitoring of aquatic en-

vironments. Lastly, fostering collaboration within the geospatial and hydrographic communities is essential. Sharing open-source tools and datasets will encourage innovation, accelerate the adoption of these techniques, and broaden their applications.

By addressing these recommendations, future work can refine and extend the utility of the proposed methodology, ensuring its continued relevance and effectiveness in hydrographic and geospatial research and applications.

## 5 Summary

This thesis explores integrating hydroacoustic and photogrammetric methods to develop a seamless Digital Bathymetric Model (DBM) for shallow and ultra-shallow water environments. The study area, Boberger See, an artificial lake in Hamburg, was selected for its suitability for testing the methodology. Data were collected using an Autonomous Hydrographic Survey Vehicle (Sonobot) equipped with a single-beam echo sounder for bathymetric measurements and a UAV with a high-resolution aerial photogrammetry camera.

The methodology involved generating Digital Elevation Models (DEMs) from the data acquired by each sensor and subsequently merging these datasets into a seamless bathymetric model. The photogrammetric data were processed using Agisoft Metashape to produce dense point clouds and DEMs. The Sonobot's measurements were interpolated for bathymetric data using the Inverse Distance Weighting (IDW) method. The integration of the datasets was achieved by employing GIS tools for seamless fusion.

The results demonstrated the feasibility and effectiveness of the approach. The UAV data provided high-resolution DEMs of ultra-shallow areas, while the Sonobot data captured the depth information for deeper sections. The final integrated model achieved high accuracy, with an RMSE value of 0.0647 m, indicating minimal error in the combined dataset. The study successfully addressed the challenges of mapping hard-to-survey areas by leveraging complementary technologies.

This research highlights the potential of integrating hydroacoustic and photogrammetric techniques for detailed and accurate bathymetric mapping. It provides a cost-effective and scalable solution for monitoring and managing aquatic environments. The findings are valuable for applications in environmental conservation, urban planning, and infrastructure development, particularly in areas where traditional survey methods face limitations. Future work could enhance the methodology by incorporating additional datasets, refining fusion algorithms, and extending the approach to diverse aquatic environments.

## 6 Appendix

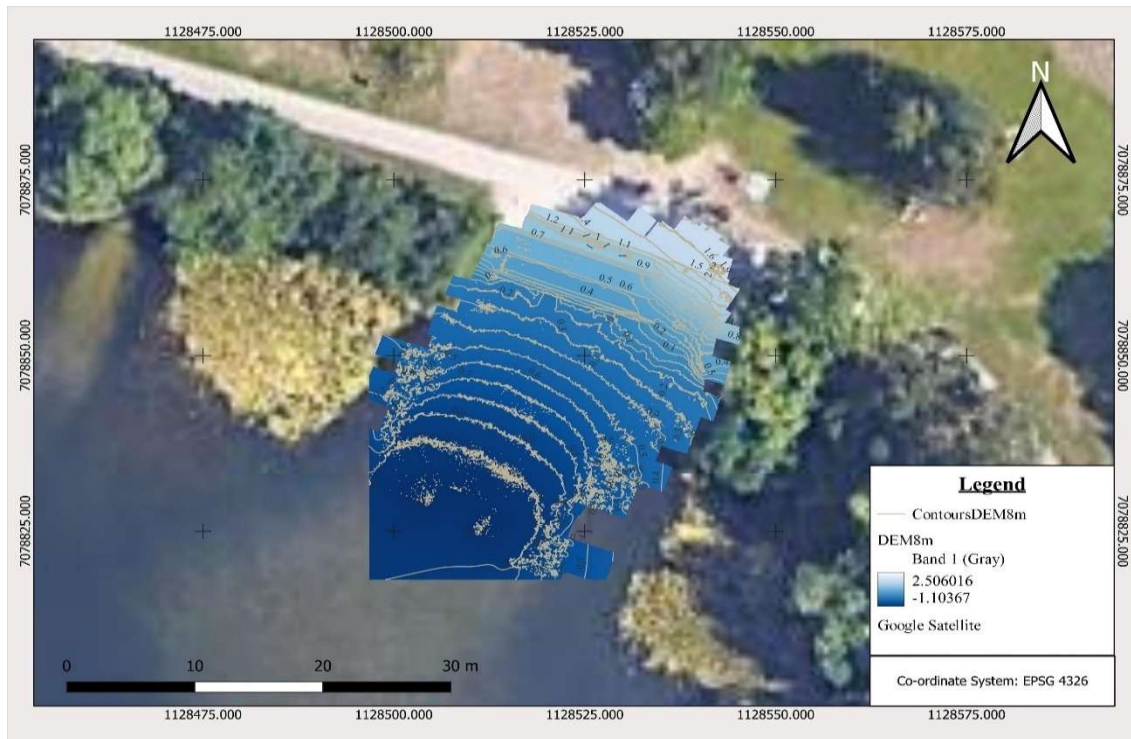


Figure 48: DEM before masking (UAV 8 m)



Figure 49: Computed Orthomosiac before masking (UAV 8 m)

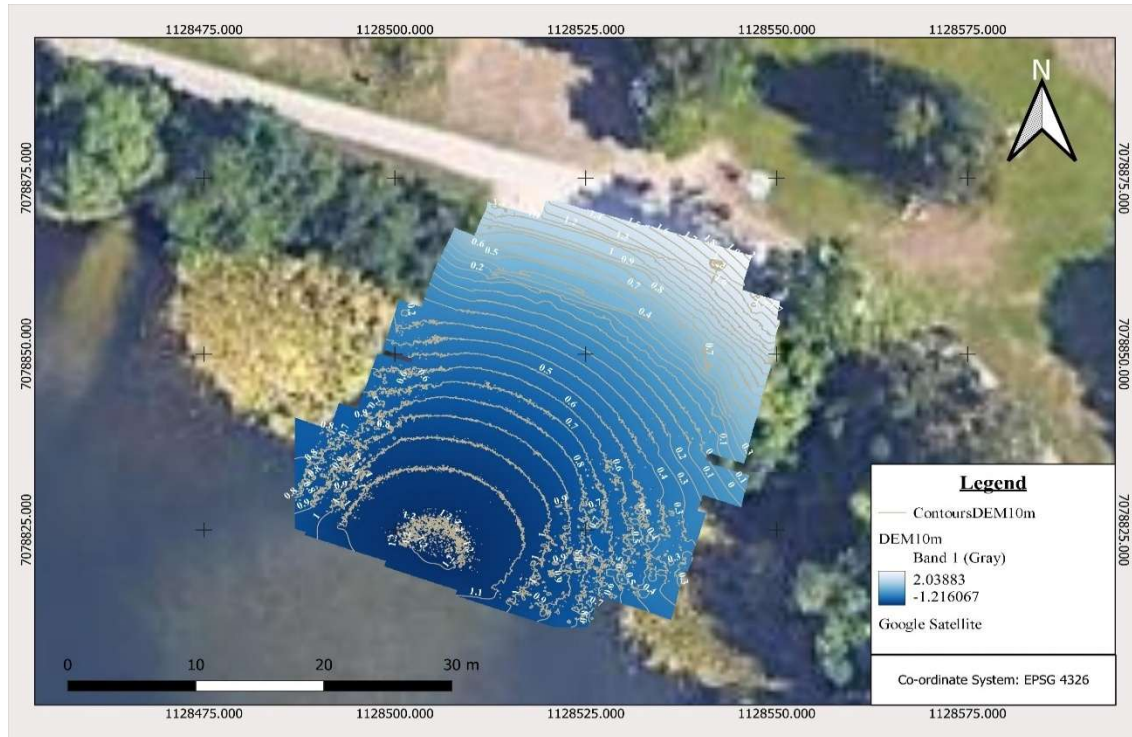


Figure 50: DEM before masking (UAV 10 m)

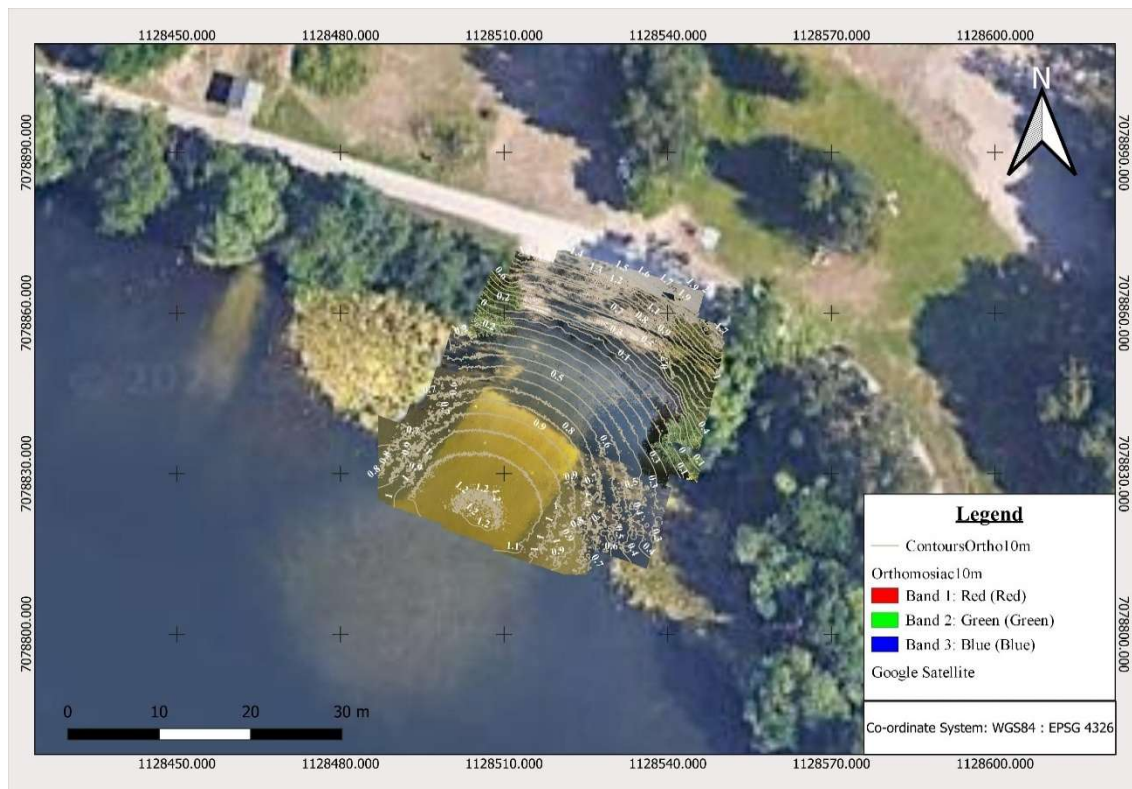


Figure 51: Computed Orthomosiac before masking (UAV 10 m)

## References

- Agisoft Metashape. (2024). *References list*. Helpdesk Portal.  
<https://agisoft.freshdesk.com/support/solutions/articles/31000156964-references-list#Align-Photos>
- Alvarez, L., Moreno, H. A., Segales, A. R., Tri Nhut Pham, Elston, J., & Jacob, J. (2018). Merging Unmanned Aerial Systems (UAS) Imagery and Echo Soundings with an Adaptive Sampling Technique for Bathymetric Surveys. *Remote Sensing*, 10(9), 1362–1362. <https://doi.org/10.3390/rs10091362>
- Ardent Training. (2024, January 4). *Boat Handling And How Bernoulli's Principle Affects This - An Ardent Training Masterclass*. YouTube.  
<https://www.youtube.com/watch?v=0-lP6ZCn0os>
- Arun, V. V., Ch. Venkateswarlu, B. Gireesh, Prasad, K. V. S. R., & Sharma, R. (2021). On improved nearshore bathymetry estimates from satellites using ensemble and machine learning approaches. *Advances in Space Research*, 68, 8.  
<https://doi.org/10.1016/j.asr.2021.06.034>
- Bahaa, S., Salem, S., & Hany, E. (2021). Accuracy Assessment of Global Bathymetry and Topography at 15 Arc Sec. (SRTM15+V2) Using Red Sea Floor Topography, Egypt. In *International Journal of Engineering Research & Technology (IJERT)*.
- Dhabban, Eng. A. (2021, January 30). *Single-Beam & Multi-Beam Echo Sounders | GrabCAD Tutorials*. Grabcad.com. <https://grabcad.com/tutorials/single-beam-multi-beam-echo-sounders>
- DJI. (2020, April 28). *Get Ready To Up Your Creative Game With The New DJI Mavic Air 2 - DJI*. DJI Official. [https://www.dji.com/newsroom/news/get-ready-to-up-your-creative-game-with-the-new-dji-mavic-air-2?as=0001&clickaid=hcLWS-CKnj2RnpFO6pvDcUUGfRnWPFXSs&clickpid=770167&clicksid=97c59d132a0c058c700fb371a187b972&from=dap\\_unique&pm=custom](https://www.dji.com/newsroom/news/get-ready-to-up-your-creative-game-with-the-new-dji-mavic-air-2?as=0001&clickaid=hcLWS-CKnj2RnpFO6pvDcUUGfRnWPFXSs&clickpid=770167&clicksid=97c59d132a0c058c700fb371a187b972&from=dap_unique&pm=custom)
- DJI. (2024). *Support for Mavic 2 - DJI*. DJI. <https://www.dji.com/de/support/product/mavic-2>
- DroneDJ. (2020, January). *DJI Mavic Air 2: reviews, features, price, etc.* DroneDJ.  
<https://dronedj.com/guides/dji-mavic-air-2/>

- E. Kasvi, Salmela, J., E. Lotsari, Kumpula, T., & Lane, S. N. (2019). Comparison of remote sensing based approaches for mapping bathymetry of shallow, clear water rivers. *Geomorphology*, 333, 180–197. <https://doi.org/10.1016/j.geomorph.2019.02.017>
- ESRI. (2024). *How inverse distance weighted interpolation works—ArcGIS Pro | Documentation*. Arcgis.com. <https://pro.arcgis.com/en/pro-app/latest/help/analysis/geostatistical-analyst/how-inverse-distance-weighted-interpolation-works.htm#GUID-3B0C89D4-1463-4570-B070-0D5CBCE540E2>
- ESRI. (2025). *Mosaic To New Raster (Data Management)—ArcGIS Pro | Documentation*. Arcgis.com. [https://pro.arcgis.com/en/pro-app/latest/tool-reference/data-management/mosaic-to-new-raster.htm#ESRI\\_US-AGES\\_DC2D04097B624DABACC65260FB723D4F](https://pro.arcgis.com/en/pro-app/latest/tool-reference/data-management/mosaic-to-new-raster.htm#ESRI_US-AGES_DC2D04097B624DABACC65260FB723D4F)
- EvoLogics . (2024). *SONOBOT System | EvoLogics*. EvoLogics. <https://www.evologics.com/sonobot-system>
- Fonstad, M. A., Dietrich, J. T., Courville, B. C., Jensen, J. L., & Carboneau, P. E. (2013). Topographic structure from motion: a new development in photogrammetric measurement. *Earth Surface Processes and Landforms*, 38(4), 421–430. <https://doi.org/10.1002/esp.3366>
- Fossen, T. I. (2011). *Handbook of Marine Craft Hydrodynamics and Motion Control*. John Wiley & Sons, Ltd. <https://doi.org/10.1002/9781119994138>
- Francois Clapuyt, Vanacker, V., & Oost, K. V. (2016). Reproducibility of UAV-based earth topography reconstructions based on Structure-from-Motion algorithms. *Geomorphology*, 260, 4–15. <https://doi.org/10.1016/j.geomorph.2015.05.011>
- Galliani, S., Lasinger, K., Photogrammetry, K., Sensing, R., & Zurich, E. (n.d.). *Massively Parallel Multiview Stereopsis by Surface Normal Diffusion*.
- Gilbertson, S. (2020, April 28). *DJI Mavic Air 2: Specs, Price, Release Date*. WIRED. <https://www.wired.com/story/dji-mavic-air-2/>
- Hamburg Tourismus. (2024). *Boberger See Hamburg*. Hamburg-Travel.com. <https://www.hamburg-travel.com/see-explore/sports-recreation/pools-wellness/boberger-lake-sandstrand/>
- Hodges, B. A., Grare, L., Greenwood, B., Matsuyoshi, K., Pizzo, N., Statom, N. M., Farrar, J. T., & Lenain, L. (2023). Evaluation of Ocean Currents Observed from

- Autonomous Surface Vehicles. *Journal of Atmospheric and Oceanic Technology*, 40(10), 1121–1136. <https://doi.org/10.1175/jtech-d-23-0066.1>
- Janowski, L., Wroblewski, R., Janusz Dworniczak, Kolakowski, M., Karolina Rogowska, Wojcik, M., & Gajewski, J. (2021). Offshore benthic habitat mapping based on object-based image analysis and geomorphometric approach. A case study from the Slupsk Bank, Southern Baltic Sea. *Science of the Total Environment*, 801, 149712. <https://doi.org/10.1016/j.scitotenv.2021.149712>
- Legleiter, C., Overstreet, B., & Kinzel, P. (2018). Sampling Strategies to Improve Passive Optical Remote Sensing of River Bathymetry. *Remote Sensing*, 10(6), 935. <https://doi.org/10.3390/rs10060935>
- Lubczonek, J., Kazimierski, W., Zaniewicz, G., & Lacka, M. (2021). Methodology for Combining Data Acquired by Unmanned Surface and Aerial Vehicles to Create Digital Bathymetric Models in Shallow and Ultra-Shallow Waters. *Remote Sensing*, 14(1), 105. <https://doi.org/10.3390/rs14010105>
- M.J. Westoby, Brasington, J., Glasser, N. F., M.J. Hambrey, & Reynolds, J. M. (2012). “Structure-from-Motion” photogrammetry: A low-cost, effective tool for geoscience applications. *Geomorphology*, 179, 300–314. <https://doi.org/10.1016/j.geomorph.2012.08.021>
- Manda, D., Thein, M.-W., D'amore, A., & Armstrong, A. (2015). *A Low Cost System for Autonomous Surface Vehicle based Hydrographic Survey*.
- Matúš Hodúl, Bird, S., Anders Knudby, & René Chénier. (2018). Satellite derived photogrammetric bathymetry. *ISPRS Journal of Photogrammetry and Remote Sensing*, 142, 268–277. <https://doi.org/10.1016/j.isprsjprs.2018.06.015>
- Mott, R. L., & Untener, J. A. (2015). *Applied fluid mechanics*. Pearson.  
<https://books.google.de/books?id=Oo8WnwEACAAJ>
- Murphy, K. (2020, April 30). *Review: The DJI Mavic Air 2 is the best all-around drone for most people*. DPReview. [https://www.dpreview.com/reviews/review-the-dji-mavic-air-2-is-the-best-all-around-drone-for-most-people?utm\\_source=chatgpt.com](https://www.dpreview.com/reviews/review-the-dji-mavic-air-2-is-the-best-all-around-drone-for-most-people?utm_source=chatgpt.com)
- Pock, T., Zebedin, L., & Bischof, H. (2011). TGV-Fusion. In Calude, Cristian S, G. Rosenberg, & A. Salomaa (Eds.), *Lecture Notes in Computer Science* (pp. 245–

- 258). Springer Berlin Heidelberg. <https://doi.org/10.1007/978-3-642-19391-0%E2%82%818>
- Puffin, S. (n.d.). *Displacement vs Planing Hulls*. [Www.youtube.com](https://www.youtube.com/watch?v=i65mI8jA96w). Retrieved February 22, 2022, from <https://www.youtube.com/watch?v=i65mI8jA96w>
- Savio, D., Torres, L., Alejandra, Rocio, S., Tania, & Neckel, A. (2023). Using UAVs and photogrammetry in bathymetric surveys in shallow waters. *Applied Sciences*, 13, 6. <https://doi.org/10.3390/app13063420>
- Sweeney, C. (n.d.). *Theia multiview geometry library: Tutorial & reference*.
- Trimble. (2024). *Trimble R980 GNSS system*. Trimble.com. <https://geospatial.trimble.com/en/products/hardware/trimble-r980>
- Vasiljevic, A., Buxton, B., Sharvit, J., Stilinovic, N., Nad, D., Miskovic, N., Planer, D., Hale, J., & Vukic, Z. (2015). *An ASV for coastal underwater archaeology: The pladypus survey of caesarea maritima, israel*. 1–7. <https://doi.org/10.1109/OCEANS-Genova.2015.7271495>
- Wilson, B., Singh, A., & Sethi, A. (2022). *Shallow water bathymetry survey using an autonomous surface vehicle*. 7898–7901. <https://doi.org/10.1109/IGARSS46834.2022.9884007>
- Woodget, A. S., Carboneau, P. E., Visser, F., & Maddock, I. P. (2014). Quantifying submerged fluvial topography using hyperspatial resolution UAS imagery and structure from motion photogrammetry. *Earth Surface Processes and Landforms*, 40(1), 47–64. <https://doi.org/10.1002/esp.3613>
- Yastrebova, A., Marko Höyhtyä, Sandrine Boumard, & Aleksandr Ometov. (2020). *Comparative study on GNSS positioning systems for autonomous vessels in the arctic region*. <https://api.semanticscholar.org/CorpusID:220096315>
- Yeu, Y., Yee, J.-J., Yun, H., & Kim, K. (2018). Evaluation of the Accuracy of Bathymetry on the Nearshore Coastlines of Western Korea from Satellite Altimetry, Multi-Beam, and Airborne Bathymetric LiDAR. *Sensors*, 18(9), 2926. <https://doi.org/10.3390/s18092926>
- Zwolak, K., Wigley, R., Bohan, A., Zarayskaya, Y., Bazhenova, E., Dorshow, W., Sumiyoshi, M., Sattiabaruth, S., Roperez, J., Proctor, A., Wallace, C., Sade, H., Ketter, T., Simpson, B., Tinmouth, N., Falconer, R., Ryzhov, I., & Elsaied Abou-Mahmoud, M. (2020). The Autonomous Underwater Vehicle Integrated

with the Unmanned Surface Vessel Mapping the Southern Ionian Sea. The Winning Technology Solution of the Shell Ocean Discovery XPRIZE. *Remote Sensing*, 12(8), 1344. <https://doi.org/10.3390/rs12081344>